J. Plasma Phys. (2025), *vol*. 91, E11
Published by Cambridge University Press

doi:10.1017/S0022377824000898

Energy flux decomposition in magnetohydrodynamic turbulence

Damiano Capocci [1], Perry L. Johnson [2], Sean Oughton [3], Luca Biferale [1] and Moritz Linkmann [4,†]

[1]Department of Physics and INFN, University of Rome Tor Vergata, Rome, Italy

[2]Department of Mechanical and Aerospace Engineering, University of California, Irvine, CA USA

[3]Department of Mathematics, University of Waikato, Hamilton, New Zealand

[4]School of Mathematics and Maxwell Institute for Mathematical Sciences, University of Edinburgh, Edinburgh EH9 3FD, UK

(Received 15 February 2024; revised 8 July 2024; accepted 30 July 2024)

In hydrodynamic (HD) turbulence, an exact decomposition of the energy flux across scales has been derived that identifies the contributions associated with vortex stretching and strain self-amplification (Johnson, *Phys. Rev. Lett.*, vol. 124, 2020 104501; *J. Fluid Mech.*, vol. 922, 2021, A3) to the energy flux across scales. Here, we extend this methodology to general coupled advection–diffusion equations and, in particular, to homogeneous magnetohydrodynamic (MHD) turbulence. We show that several MHD subfluxes are related to each other by kinematic constraints akin to the Betchov relation in HD. Applied to data from direct numerical simulations, this decomposition allows for an identification of physical processes and for the quantification of their respective contributions to the energy cascade, as well as a quantitative assessment of their multi-scale nature through a further decomposition into single- and multi-scale terms. We find that vortex stretching is strongly depleted in MHD compared with HD, and the kinetic energy is transferred from large to small scales almost exclusively by the generation of regions of small-scale intense strain induced by the Lorentz force. In regions of large strain, current sheets are stretched by large-scale straining motion into regions of magnetic shear. This magnetic shear in turn drives extensional flows at smaller scales. Magnetic energy is transferred from large to small scales predominantly by the aforementioned current-sheet thinning in regions of high strain. The contributions from current-filament stretching – the analogue to vortex stretching – and from bending of magnetic field-lines into current filaments by vortical motion are both almost negligible, although the latter induces strong backscatter of magnetic energy. Consequences of these results for subgrid-scale turbulence modelling are discussed.

Keywords: plasma flows

† Email address for correspondence: Moritz.Linkmann@ed.ac.uk

1. Introduction

Turbulence in electrically conducting fluids and plasmas is of relevance to a variety of processes in geophysical and astrophysical situations, as well as in industry (Weiss & Proctor 2014; Davidson 2016) and for nuclear fusion under magnetic confinement. For example, the solar wind is turbulent (Bruno & Carbone 2013), convection-driven turbulence occurs in planetary cores and in the outer layers of stars (Jones 2011), turbulence on ion and electron scales affects plasma confinement in magnetic confinement fusion reactors (Freidberg 2007), and the heat transfer in liquid metal cooling applications is dependent on the level of turbulence in the flow (Davidson 1999). Even though these systems are very different in terms of features like the presence of strong background magnetic fields, the level of magnetic field fluctuations, temperature gradients, density fluctuations, domain geometry or the level of collisionality, they nonetheless share fundamental nonlinear processes that define energy conversion and inter-scale energy transfers, at least on scales where the fluid approximation is applicable. Even in the simplest case of magnetohydrodynamic (MHD) turbulence, despite considerable theoretical progress (e.g. Goldreich & Sridhar 1995; Biskamp 2003; Zhou, Matthaeus & Dmitruk 2004; Petrosyan *et al.* 2010; Brandenburg, Sokoloff & Subramanian 2012; Tobias & Cattaneo 2013; Beresnyak 2019; Oughton & Matthaeus 2020; Schekochihin 2022), the physical nature of these processes remain opaque.

Moreover, the typical parameter ranges in which MHD turbulence develops in Nature are far from those attainable with direct numerical simulation (DNS) (Plunian, Stepanov & Frick 2013; Miesch *et al.* 2015; Schmidt 2015). As a consequence, the demand for approximations and subgrid-scale (SGS) models for large-eddy simulation (LES) of MHD turbulence that are able to capture the effects of unresolved small-scale fluctuations – that govern important processes such as magnetic reconnection and plasma heating – is increasing (Miesch *et al.* 2015). However, constructing such models is a challenge due to small-scale anisotropy (Shebalin, Matthaeus & Montgomery 1983; Oughton, Priest & Matthaeus 1994; Goldreich & Sridhar 1997; Tobias & Cattaneo 2013), strong intermittency in the magnetic fluctuations as observed in numerical simulations (e.g. Mininni & Pouquet 2009; Sahoo, Perlekar & Pandit 2011; Yoshimatsu *et al.* 2011; Rodriguez Imazio *et al.* 2013; Meyrand, Kiyani & Galtier 2015) and in the solar wind (e.g. Veltri 1999; Salem *et al.* 2009; Wan *et al.* 2012; Matthaeus *et al.* 2015), insufficient magnetic-field amplification and dynamo growth observed in LES of MHD turbulence (Haugen & Brandenburg 2006), and whether magnetic-field fluctuations are maintained by the flow or by an external electromagnetic force (Alexakis & Chibbaro 2022). For a summary of the SGS modelling effort and its challenges, we refer to the review articles by Miesch *et al.* (2015) and Schmidt (2015).

Here, we focus on energy transfer across scales in statistically stationary homogeneous MHD turbulence in a saturated nonlinear dynamo regime without a mean magnetic field, and with negligible levels or cross- and magnetic helicity. The total energy cascade in this case is direct (Aluie & Eyink 2010), transferring energy from the large to the small scales in a scale-local fashion. Herein, we use the term cascade to indicate a mean flux and refer to pointwise upscale and downscale energy transfers as inverse and direct transfer events, respectively, or in the former case also as backscatter. The aims of this paper are: (i) to understand the physical mechanisms that govern the MHD energy cascade and (ii) to quantify their importance and provide guidance for SGS modelling (Johnson 2022). In terms of turbulence theory, this corresponds to understanding physical properties of the SGS stresses as a function of scale. Eyink (2006) introduced a viable approach for this that involves expanding the SGS tensors in terms

https://doi.org/10.1017/S0022377824000898 Published online by Cambridge University Press

of vector field gradients. Here, we follow a filtering approach, generalising an exact gradient-based decomposition of the hydrodynamic (HD) energy fluxes (Johnson 2020, 2021) to coupled advection–diffusion equations and hence to the MHD equations. This methodology distinguishes between terms that are local in scale, corresponding to the first term in the gradient expansion and those which are truly multi-scale, providing a closed expression for the remainder of the series expansion. Expressing SGS stresses through vector-field gradients results in a decomposition of the energy fluxes in terms of different tensorial contractions between strain-rate, vorticity, current and magnetic strain, and as such facilitates the physical interpretation of such sub-fluxes. The provision of closed expressions allows for a quantification of the relative contribution of all terms to the energy cascade using data obtained by direct numerical simulation (DNS). In homogeneous and isotropic HD turbulence, where only the inertial term is present, the decomposition identifies three processes that transfer kinetic energy across scales, vortex stretching, strain self-amplification and strain-vorticity alignment, and quantifies their relative contribution to the energy cascade (Johnson 2020, 2021). Similarly, the direct cascade of kinetic helicity is carried by three different processes, vortex flattening, vortex twisting and vortex entanglement (Capocci *et al.* 2023).

In MHD, the total energy transfer can be split into four subfluxes, Inertial, Maxwell, Dynamo and Advection,[1] with the former two originating from the Reynolds and Maxwell stresses in the momentum equation, and the latter two from stresses in the induction equation that result in the advection and bending/stretching of magnetic field lines by the flow. As Dynamo and Advection terms have a common physical origin, the electric field, often only their sum is considered in *a priori* analyses of DNS data (Aluie 2017; Offermans *et al.* 2018; Alexakis & Chibbaro 2022) and *a posteriori* in LES (Zhou & Vahala 1991; Müller & Carati 2002; Grete *et al.* 2016; Kessar, Balarac & Plunian 2016; Vlaykov *et al.* 2016). However, in the present work, it will prove instructive to consider them separately. Here, we generalise and apply the aforementioned decomposition to each of these four subfluxes.

In doing so, we identify a single process, current-sheet thinning, to be the main contributor to the forward cascade of magnetic energy. Contributions from strain-induced current-filament stretching, the formal analogue to vortex stretching, are subdominant. Furthermore, we find that vortex-stretching and strain self-amplification are strongly suppressed at all length scales. Instead the back-reaction of current-sheet thinning on the flow through the Lorentz force constitutes the main transfer of kinetic energy from large to small scales, with contributions related to current-filament stretching turning out to be negligible.

The structure of the paper is as follows: we begin in § 2 with an outline of how the generalised method can be applied to obtain MHD energy subfluxes. In § 3, we discuss the numerical details and the associated datasets on which we performed the filtering analysis. In § 4, we consider each subflux decomposition, showing results for both mean terms and fluctuations. Ramifications of those results for SGS modelling are considered in § 5. In § 6, we discuss our main results and indicate future work directions. Several appendices flesh out some aspects of the derivations and analysis.

2. Theory

In this section, we begin by sketching the derivation of the coarse-grained energy equations for MHD and giving the definitions of the scale-space energy fluxes that appear

[1]We use these words capitalised to indicate that they refer to the SGS energy flux arising from the term with the lowercase version of the name in the momentum or induction equation.

https://doi.org/10.1017/S0022377824000898 Published online by Cambridge University Press

in them. Subsequently, we show how each flux can be decomposed in terms of physically distinct contributions, and discuss their physical interpretations.

2.1. *Coarse-grained energy equations*

Our starting point is incompressible three-dimensional (3-D) homogeneous MHD turbulence. The primary dynamical variables are then the fluctuation velocity $\boldsymbol{u}(\boldsymbol{x}, t)$ and the fluctuation magnetic field $\boldsymbol{b}(\boldsymbol{x}, t)$, where we measure the latter in Alfvén speed units: $\boldsymbol{b}/\sqrt{4\pi\rho} \to \boldsymbol{b}$, with ρ the uniform mass density. We consider situations with no mean magnetic field since these are more likely to exhibit global isotropy. The governing equations, with allowance for hyper-dissipation, are

$$\partial_t u_i + \partial_j \left(u_i u_j\right) = -\partial_i \left(p + \frac{b^2}{2}\right) + \partial_j \left(b_i b_j\right) + \nu_\alpha (-1)^{\alpha+1} \nabla^{2\alpha} u_i + F_i, \tag{2.1}$$

$$\partial_t b_i + \partial_j \left(b_i u_j\right) = \partial_j \left(u_i b_j\right) + \mu_\alpha (-1)^{\alpha+1} \nabla^{2\alpha} b_i, \tag{2.2}$$

$$\boldsymbol{\nabla} \cdot \boldsymbol{u} = 0, \quad \boldsymbol{\nabla} \cdot \boldsymbol{b} = 0. \tag{2.3}$$

Here, p is the pressure, $\boldsymbol{F}$ is a (large-scale) velocity forcing, ν_α and μ_α are the hyper-viscosity and hyper-resistivity, and α denotes the power of the Laplacian operator employed in the hyper-dissipation. Standard Laplacian dissipation corresponds to the case $\alpha = 1$.

The MHD variables, and equations, may be spatially coarse-grained using a suitable filtering field, $G^\ell(\boldsymbol{r})$ (Germano 1992; Aluie 2017). The role of $G^\ell(\boldsymbol{r})$ is to strongly suppresses structure at scales less than the filtering scale ℓ. For example, the filtered velocity field is

$$\bar{\boldsymbol{u}}^\ell(\boldsymbol{x}) = \int \mathrm{d}\boldsymbol{r}\, G^\ell(\boldsymbol{r})\, \boldsymbol{u}(\boldsymbol{x} + \boldsymbol{r}). \tag{2.4}$$

This can be interpreted as a weighted average of $\boldsymbol{u}$ centred on the position $\boldsymbol{x}$. The weighting function G^ℓ decays very rapidly to zero at distances greater than a few ℓ from $\boldsymbol{x}$ and satisfies some other weak restrictions, such as smoothness and having a volume integral of unity. Filtering is a linear operation and commutes with differentiation, properties of which we will make considerable use below. From § 2.2 onwards, we will specialise to a Gaussian filter, but in this section, a specific choice of filter is not needed.

Coarse-graining of (2.1)–(2.2) introduces four SGS stress tensors, $\tau^\ell(\cdot, \cdot)$, associated with the advective-type nonlinear terms (those containing a ∂_j). These each have the form

$$\tau^\ell(f_i, g_j) = \overline{f_i g_j}^\ell - \bar{f}_i^\ell\, \bar{g}_j^\ell, \tag{2.5}$$

where $\boldsymbol{f}$ and $\boldsymbol{g}$ are the solenoidal vectors appearing in a $g_j \partial_j f_i$ advective-type term. We remark that with this notation, the advecting field is the second argument in a $\tau^\ell(\cdot, \cdot)$.

To obtain the equations governing the (pointwise) evolution of the coarse-grained kinetic energy $E_u^\ell(\boldsymbol{x}, t) = \frac{1}{2}\bar{\boldsymbol{u}}^\ell \cdot \bar{\boldsymbol{u}}^\ell$ and magnetic energy $E_b^\ell(\boldsymbol{x}, t) = \frac{1}{2}\bar{\boldsymbol{b}}^\ell \cdot \bar{\boldsymbol{b}}^\ell$, one filters (2.1)–(2.2) and then multiplies by $\bar{\boldsymbol{u}}^\ell$ and $\bar{\boldsymbol{b}}^\ell$, respectively (e.g. Zhou & Vahala 1991; Kessar *et al.* 2016; Aluie 2017; Offermans *et al.* 2018; Alexakis & Chibbaro 2022). The result can be written as

$$\partial_t E_u^\ell + \boldsymbol{\nabla} \cdot \boldsymbol{\mathcal{J}}_u = -\Pi^{I,\ell} - \Pi^{M,\ell} - \mathcal{W}^\ell - \mathcal{D}_u + \bar{\boldsymbol{u}}^\ell \cdot \bar{\boldsymbol{F}}^\ell, \tag{2.6}$$

$$\partial_t E_b^\ell + \boldsymbol{\nabla} \cdot \boldsymbol{\mathcal{J}}_b = -\Pi^{A,\ell} - \Pi^{D,\ell} + \mathcal{W}^\ell - \mathcal{D}_b, \tag{2.7}$$

where the $\boldsymbol{\mathcal{J}}$ terms account for the spatial transport of energy and the Π^ℓ terms embody energy fluxes (i.e. transfer across scale ℓ). Our sign convention for the definitions of the

https://doi.org/10.1017/S0022377824000898 Published online by Cambridge University Press

Π^ℓ (see below) means that $\Pi^\ell > 0$ corresponds to forward transfer of energy, i.e. to scales smaller than ℓ. The $\mathcal{D}$ terms represent (hyper-)dissipative effects. Also present is the resolved scale conversion (RSC) term, $\mathcal{W}^\ell = \bar{b}_i^\ell \bar{b}_j^\ell \partial_j \bar{u}_i^\ell$, here expressed as in Aluie (2017). This appears with opposite sign in each equation, and represents an *exchange* between large-scale kinetic and magnetic energies. An important point is that it is not an energy flux term since it does not involve energy transfer across scale ℓ. It supports several interpretations including as: (i) the rate of work done on the large-scale flow by the large-scale Lorentz force and (ii) the energy gained by $\bar{\boldsymbol{b}}^\ell$ as it is distorted by $\bar{\boldsymbol{u}}^\ell$ or *vice versa*. Detailed forms for the spatial transport currents, $\mathcal{J}_u, \mathcal{J}_b$, depend on the form employed for $\mathcal{W}^\ell$ and are available elsewhere (e.g. Kessar *et al.* 2016; Aluie 2017; Offermans *et al.* 2018; Alexakis & Chibbaro 2022), while the problem of Galilean invariance has been addressed by Offermans *et al.* (2018).

Our primary interest herein centres on the pointwise energy flux (at scale ℓ) terms, denoted by $\Pi^\ell(\boldsymbol{x}, t)$, together with their volume averages, $\langle \Pi^\ell \rangle$. For any choice of filter, these can be expressed in terms of contractions of filtered gradient tensors and SGS stress tensors:

$$\Pi^{I,\ell} = -\frac{\partial \bar{u}_i^\ell}{\partial x_j} \tau^\ell(u_i, u_j), \tag{2.8}$$

$$\Pi^{M,\ell} = \frac{\partial \bar{u}_i^\ell}{\partial x_j} \tau^\ell(b_i, b_j), \tag{2.9}$$

$$\Pi^{A,\ell} = -\frac{\partial \bar{b}_i^\ell}{\partial x_j} \tau^\ell(b_i, u_j), \tag{2.10}$$

$$\Pi^{D,\ell} = \frac{\partial \bar{b}_i^\ell}{\partial x_j} \tau^\ell(u_i, b_j). \tag{2.11}$$

Like the $\tau^\ell(\cdot, \cdot)$, these arise in connection with the four advection type nonlinearities in (2.1)–(2.2) that we refer to as the Inertial, Maxwell (meaning from the Lorentz force), Advection and Dynamo terms. Note the capitalisation. Taken together with (2.6) and (2.7), these definitions of the Π^ℓ terms mean that the interpretation of the direction of an energy flux does not depend on which flux it is. This is why (2.9) and (2.11) lack a leading minus sign. Specifically, a positive value for any one of these fluxes corresponds to transfer of energy from scales greater than ℓ to scales smaller than ℓ. Clearly, $\Pi^{I,\ell} + \Pi^{M,\ell}$ is the net flux of E_u^ℓ, and $\Pi^{A,\ell} + \Pi^{D,\ell}$ that for E_b^ℓ. As is well known, $\Pi^{A,\ell}$ and $\Pi^{D,\ell}$ have a common origin and may be readily combined to obtain the magnetic energy flux associated with the curl of the induced electric field.

We remark that energy transfer in MHD turbulence has traditionally been discussed in a Fourier-space approach (e.g. Dar, Verma & Eswaran 2001; Verma 2004; Alexakis, Mininni & Pouquet 2005; Mininni, Montgomery & Pouquet 2005; Teaca *et al.* 2009; Linkmann *et al.* 2017; Verma 2019). The filtering approach used here results in equivalent expressions for the mean inertial flux if the filter is chosen to be a Galerkin projector. However, in MHD, the two approaches differ in important details. In the Fourier-space approach, the transfer terms originating from the Lorentz force (momentum equation) and the field-line stretching term (induction equation) retain contributions that only involve a coupling among resolved scales. That is, the RSC term $\mathcal{W}^\ell$ is not separated out from the fluxes. This is the reason these terms do not vanish in the limit of $k \to \infty$ in the Fourier-based approach, in contrast to the terms defined in (2.8)–(2.11) using the SGS stresses, which therefore are genuine flux terms. As a consequence, the Fourier-based

https://doi.org/10.1017/S0022377824000898 Published online by Cambridge University Press

definitions can result in misinterpretations of the multi-scale nature of kinetic-to-magnetic energy conversion and of the role of the Lorentz force in inducing kinetic energy transfer across scales. For further details, see the works of Aluie (2017) and Offermans *et al.* (2018). An in-depth discussion of the SGS-based definition of energy flux and a comparison with the Fourier-based approach is supplied by Aluie & Eyink (2009).

2.2. *Gaussian filter*

Rather remarkably, the choice of a Gaussian filter enables an analytic determination of the SGS stresses and fluxes in terms of field gradients with contributions from the resolved scales and the subfilter scales. In the remainder of the paper, we therefore employ an isotropic Gaussian filter

$$G^\ell(\boldsymbol{r}) = \frac{1}{(2\pi\ell^2)^{3/2}} \exp\left(-\frac{|\boldsymbol{r}|^2}{2\ell^2}\right). \tag{2.12}$$

2.3. *Exact expressions for the τ^ℓ and Π^ℓ*

Employing the Fourier transform of the Gaussian filter (2.12), Johnson (2020, 2021) showed that the filtered version of an arbitrary field $\boldsymbol{u}(\boldsymbol{x}, t)$ satisfies a diffusion equation,

$$\frac{\partial \bar{u}_j^\ell}{\partial(\ell^2)} = \frac{1}{2}\nabla^2 \bar{u}_j^\ell, \quad \bar{u}_j^\ell\big|_{\ell=0} = u_j(\boldsymbol{x}, t), \tag{2.13}$$

where ℓ^2 is the time-like variable. It was further shown that the associated SGS stress tensor, $\tau^\ell(u_i, u_j)$, obeys a forced version of this diffusion equation. The forcing term is $\bar{A}_{ik}^\ell \bar{A}_{jk}^\ell$, where $\bar{A}_{ik}^\ell = \partial_k \bar{u}_i^\ell$ is the gradient tensor for the filtered field. An exact solution for $\tau^\ell(u_i, u_j)$ was obtained that depends on $\bar{A}_{ik}^\phi$ for all scales $\phi \le \ell$. Substituting this into the equation for the SGS Inertial flux, (2.8), produces an exact solution for this flux corresponding to the exact summation of the perturbation series proposed by Eyink (2006).

Happily, this approach is readily extended to MHD and may be used to calculate the elements contained in (2.8)–(2.11). Below, we outline how to achieve this for the particular case of the magnetic energy subflux (2.10) that originates with the advection term in the induction equation (i.e. $\boldsymbol{u}\cdot\nabla\boldsymbol{b}$). More details, plus the general case of three distinct solenoidal fields, are available in Appendix A; see also Appendix C and Capocci *et al.* (2023).

We seek an exact solution for $\tau^\ell(b_i, u_j) = \overline{b_i u_j}^\ell - \overline{b}_i^\ell \overline{u}_j^\ell$. Clearly, $\overline{b_i u_j}^\ell$ will also satisfy (2.13) since that equation holds for any (Gaussian) filtered field. Together with the product rule expansion of $\partial(\bar{b}_i^\ell \bar{u}_j^\ell)/\partial\ell^2$, this yields

$$\left(\frac{\partial}{\partial\ell^2} - \frac{1}{2}\nabla^2\right)\tau^\ell(b_i, u_j) = \bar{B}_{ik}^\ell \bar{A}_{jk}^\ell, \quad \tau^{\ell=0}(b_i, u_j) = 0, \tag{2.14}$$

where $\bar{B}_{ik}^\ell = \partial_k \bar{b}_i^\ell$ is the gradient tensor for $\bar{b}_i^\ell$. The solution can be written in the form

$$\tau^\ell(b_i, u_j) = \ell^2\, \bar{B}_{ik}^\ell \bar{A}_{jk}^\ell + \int_0^{\ell^2} \mathrm{d}\theta \left(\overline{\overline{B}_{ik}^{\sqrt{\theta}}\, \overline{A}_{jk}^{\sqrt{\theta}}}^{\phi} - \overline{\overline{B}_{ik}^{\sqrt{\theta}}}^{\phi}\, \overline{\overline{A}_{jk}^{\sqrt{\theta}}}^{\phi}\right), \tag{2.15}$$

where $\phi = \sqrt{\ell^2 - \theta}$. The first term on the right-hand side is a 'single-scale' piece as it contains only resolved scale terms (cf. Clark, Ferziger & Reynolds 1979). In terms of

https://doi.org/10.1017/S0022377824000898 Published online by Cambridge University Press

other work, it corresponds to the nonlinear model employed by Leonard (1975), Borue & Orszag (1998) and Meneveau & Katz (2000), and is the first-order term in the expansion of Eyink (2006). It is also the leading-order term of the power law expansion in the filter limit going to zero relative of any filter kernel with finite moments (cf. § 13.4.4 of Pope 2000).

The second term, involving an integral over all scales smaller than ℓ, is manifestly a multi-scale contribution that includes subfilter-scale field gradients. Note that the integrand in (2.15) can itself be written as an SGS stress, but one based on the field gradients rather than the fields themselves: $\tau^{\phi}(\bar{B}_{ik}^{\sqrt{\theta}}, \bar{A}_{jk}^{\sqrt{\theta}})$.

Contracting with $\bar{B}_{ij}^{\ell}$ provides an exact expression for (2.10):

$$\Pi^{A,\ell} = -\ell^2\, \bar{B}_{ij}^{\ell}\bar{B}_{ik}^{\ell}\bar{A}_{jk}^{\ell} - \bar{B}_{ij}^{\ell}\int_0^{\ell^2} \mathrm{d}\theta \left(\overline{\overline{B_{ik}}^{\sqrt{\theta}}\,\overline{A_{jk}}^{\sqrt{\theta}}}^{\phi} - \overline{\overline{B_{ik}}^{\sqrt{\theta}}}^{\phi}\,\overline{\overline{A_{jk}}^{\sqrt{\theta}}}^{\phi} \right) \tag{2.16}$$

$$= \Pi_s^{A,\ell} + \Pi_m^{A,\ell}, \tag{2.17}$$

where the subscripts s and m denote the single- and multi-scale contributions, respectively. It is evident that all the SGS energy fluxes, (2.8)–(2.11), and also other SGS fluxes (e.g. for helicities), can be written strictly in terms of (multi-scale) gradients of the velocity and magnetic vector fields. Appendix A contains further details. When discussing the individual SGS energy fluxes in § 4, we will make regular reference to (A3), the generalised form of (2.17).

The tensor contractions present in (2.17) can be expressed as the trace of the matrix products involved, after appropriate use of the transpose operation (superscript t). For example, $\bar{B}_{ij}^{\ell}\bar{B}_{ik}^{\ell}\bar{A}_{jk}^{\ell} = \mathrm{Tr}\left\{(\bar{\boldsymbol{B}}^{\ell})^t\,\bar{\boldsymbol{B}}^{\ell}(\bar{\boldsymbol{A}}^{\ell})^t\right\}$.

Further insight into the physics of the scale-space flux $\Pi^{A,\ell}$ may be extracted by expressing each gradient tensor as the sum of its index-symmetric and index-antisymmetric components. Let us write $S_{ij} = (A_{ij} + A_{ji})/2$ and $\Omega_{ij} = (A_{ij} - A_{ji})/2$, respectively the (velocity) rate-of-strain tensor and the rotation rate tensor, with $\Omega_{ij} = -\epsilon_{ijk}\omega_k/2$ in terms of the vorticity $\omega_k = \epsilon_{ijk}\partial_i u_j$. Similarly, $B_{ij} = \Sigma_{ij} + J_{ij}$, where the non-zero elements of $J_{ij} = (B_{ij} - B_{ji})/2 = -\epsilon_{ijk}j_k/2$ are essentially the components of the electric current density $\boldsymbol{j} = \boldsymbol{\nabla}\times\boldsymbol{b}$ and the magnetic strain-rate tensor $\Sigma_{ij} = (B_{ij} + B_{ji})/2$. We will of course require the filtered versions of all of these quantities.

Ostensibly, this decomposition gives eight single-scale and eight multi-scale sub-fluxes; see (A7). However, properties of the trace of particular products of symmetric or antisymmetric matrices mean some of these may vanish, cancel or be equivalent. In the present case, one obtains, in connection with the single-scale contributions,

$$\mathrm{Tr}\left\{\left(\bar{\mathbf{B}}^{\ell}\right)^t\,\bar{\mathbf{B}}^{\ell}\,\left(\bar{\mathbf{A}}^{\ell}\right)^t\right\} = \mathrm{Tr}\left\{\left(\bar{\boldsymbol{\Sigma}}^{\ell} - \bar{\mathbf{J}}^{\ell}\right)\left(\bar{\boldsymbol{\Sigma}}^{\ell} + \bar{\mathbf{J}}^{\ell}\right)\left(\bar{\mathbf{S}}^{\ell} - \bar{\boldsymbol{\Omega}}^{\ell}\right)\right\} \tag{2.18}$$

$$= \mathrm{Tr}\left\{\bar{\boldsymbol{\Sigma}}^{\ell}\bar{\boldsymbol{\Sigma}}^{\ell}\bar{\mathbf{S}}^{\ell} - \bar{\mathbf{J}}^{\ell}\bar{\mathbf{J}}^{\ell}\bar{\mathbf{S}}^{\ell} + 2\bar{\boldsymbol{\Sigma}}^{\ell}\bar{\mathbf{J}}^{\ell}\bar{\mathbf{S}}^{\ell}\right\}, \tag{2.19}$$

so that there are only three distinct subfluxes; see Appendix A for details. We write the single-scale flux for the Advection term as

$$\Pi_s^{A,\ell} = \Pi_{s,\Sigma\Sigma S}^{A,\ell} + \Pi_{s,JJS}^{A,\ell} + 2\Pi_{s,\Sigma JS}^{A,\ell}, \tag{2.20}$$

where $\Pi_{s,PQR}^{A,\ell} = -\ell^2\mathrm{Tr}\left\{(\bar{\mathbf{P}}^{\ell})^t\bar{\mathbf{Q}}^{\ell}(\bar{\mathbf{R}}^{\ell})^t\right\}$ and each of $\mathbf{P}, \mathbf{Q}, \mathbf{R}$ are either symmetric or antisymmetric tensors.

https://doi.org/10.1017/S0022377824000898 Published online by Cambridge University Press

id	N	α	E_u	E_b	ν_α	ε_u	ε_b	L_u	τ	**Re**	η_α / 10^{-3}	$k_{max}\,\eta^u_\alpha$	$k_{max}\,\eta^b_\alpha$	Δt / τ	#
A1	2048	5	0.66	0.54	.	0.33	0.43	0.51	0.81	9931	2.0	1.38	1.37	1.1	18
H2	2048	4	3.84	—	.	1.50	—	1.10	0.69	26000	2.3	1.57	—	1.0	6

TABLE 1. Simulation parameters and key observables, where N is the number of collocation points in each coordinate, α is the power of ∇^2 used in the hyper-diffusion, E_u the (mean) total kinetic energy, ν_α the kinematic hyperdiffusivity, ε_u and ε_b are the kinetic and magnetic energy dissipation rates, $L_u = (3\pi/4E_u)\int_0^{k_{\max}} \mathrm{d}k E_u(k)/k$ the longitudinal integral scale, $\tau = L_u/\sqrt{2E_u/3}$ the large-scale eddy-turnover time, and Re is the Reynolds number. Furthermore, $\eta_\alpha = (\nu_\alpha^3/\varepsilon)^{1/(6\alpha-2)}$, $\eta^u_\alpha = (\nu_\alpha^3/\varepsilon_u)^{1/(6\alpha-2)}$ and $\eta^b_\alpha = (\mu_\alpha^3/\varepsilon_b)^{1/(6\alpha-2)}$ are the hyperdiffusive Kolmogorov scales calculated with respect to the total, viscous and Joule dissipation rates, respectively, $k_{\max}$ the largest retained wavenumber component after de-aliasing, Δt the mean of the snapshots sampling intervals, and # indicates the number of snapshots used in the averaging. The magnetic Prandtl number, $Pm = \nu_\alpha/\mu_\alpha$, the ratio between the hyperviscosity and magnetic hyperdiffusivity, equals unity for A1.

The multi-scale flux contributions which explicitly contain subfilter-scale fluctuations can also be so decomposed, with the details given in Appendix A. The particular forms for $\Pi^{A,\ell}_m$ are discussed in § 4.3.

3. Methods and data

To quantify the four energy fluxes $\Pi^{Y,\ell}$ present in (2.6)–(2.7), and their decompositions, we employ outputs from numerical simulations of the MHD equations (2.1)–(2.3). To obtain an appreciable inertial range, we use hyperdiffusion ($\alpha = 5$), a comparison with standard diffusive MHD ($\alpha = 1$) is provided in Appendix E, always with $\nu_\alpha = \mu_\alpha$. The fluctuation fields, $\boldsymbol{u}$ and $\boldsymbol{b}$, have zero means and there is no background magnetic field (i.e. $B_0 = 0$). The equations are solved using fully dealiased Fourier pseudospectral codes in a triply periodic $(2\pi)^3$ domain (Patterson & Orszag 1971; Canuto *et al.* 1988). The time advancement is via a second-order Runge–Kutta scheme with dealiasing implemented using the two-thirds rule.

As table 1 indicates, we use up to 2048^3 grid points. The spatial resolution of the simulations is quantified by both the grid spacing $\Delta x = 2\pi/N$ and the hyper-diffusive Kolmogorov scales $\eta^u_\alpha = (\nu_\alpha^3/\varepsilon_u)^{1/(6\alpha-2)}$ and $\eta^b_\alpha = (\mu_\alpha^3/\varepsilon_b)^{1/(6\alpha-2)}$, where ε_u and ε_b are the mean kinetic and magnetic energy dissipation rates (Borue & Orszag 1995). For adequate resolution, we require $\eta^u_\alpha/\Delta x \gtrsim 1.3$ and $\eta^b_\alpha/\Delta x \gtrsim 1.3$ (e.g. Donzis, Yeung & Sreenivasan 2008; Wan *et al.* 2010).

The forcing f applied to the system is a drag-free Ornstein–Uhlenbeck process, active in the wavenumber band $k \in [2.5, 5.0]$ for the MHD simulations, while the hydrodynamics dataset H2 is forced in the band $k \in [0.5, 1.5]$. The snapshots, consisting of instantaneous velocity and magnetic fields, have been sampled about once per large-scale turnover time after the simulations reach statistically stationary states.

Figure 1 shows the time-averaged omnidirectional kinetic and magnetic spectra. The peak in the kinetic spectrum is due to the activity of forcing for $k \in [2.5, 5.0]$, while the magnetic spectrum is considerably lower over that interval since the induction equation is not forced. In the (approximate) inertial range, both spectra have approximately power law scaling, with $E_b(k)$ close to $k^{-5/3}$ and $E_u(k)$ significantly shallower. As is typically seen in MHD simulations with no mean field, the Alfvén ratio, $E_u(k)\,/\,E_b(k)$, is less than unity in the inertial range, i.e. magnetic energy predominates at these scales.

https://doi.org/10.1017/S0022377824000898 Published online by Cambridge University Press

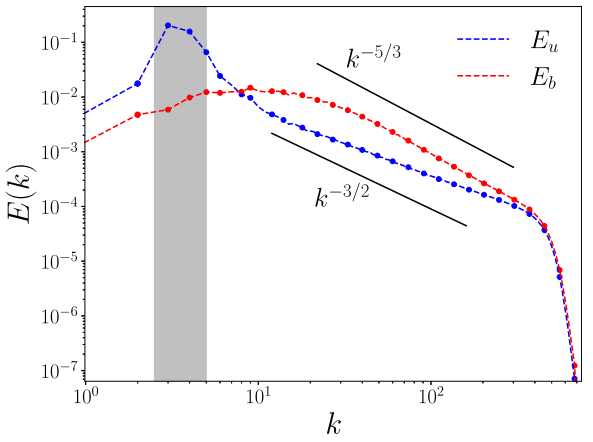

FIGURE 1. Time-averaged omnidirectional spectra for the velocity and magnetic field (run A1). The grey region indicates the wavenumber band where the velocity field is forced: $k \in [2.5, 5.0]$.

At high k, there is a steep and roughly coincident decrease of both spectra. This is a consequence of two factors. First, the employment of hyperviscosity makes the dissipation range more concentrated in the small scales, leading to the sharp fall-off. Second, unit Prandtl number ensures that the dissipation wavenumber band is the same for the kinetic and magnetic spectra. Note the clear superequipartition in the entire scaling range of the spectra, with $E_b(k) > E_u(k)$ for $10 \leq k \leq 400$. Equipartition at large k in the inertial range as previously predicted for decaying turbulence (Müller & Grappin 2004; Haugen & Brandenburg 2006) is not observed, however, as $E_b(k)$ is steeper than $E_u(k)$ it does approach $E_u(k)$ resulting in approximate equipartition in the dissipative range.

To calculate an effective Reynolds number for a hyperdissipative system, we follow the approach described by Buzzicotti *et al.* (2018). There, the standard (Laplacian dissipation) integral-scale Reynolds number $Re = UL_u / \nu \propto (L_u / \eta_2)^{4/3}$ (e.g. Batchelor 1970; Pope 2000) is replaced with one based on the ratio between the integral scale L_u and the effective dissipation range scale I_d. Specifically, we employ

$$Re = C \left(\frac{L_u}{I_d} \right)^{4/3}, \tag{3.1}$$

where $I_d = \pi \,/\, \mathrm{argmax}\left(k^2 E_u(k)\right)$ is the scale where the dissipation spectrum $k^2 E_u(k)$ has a maximum. Here, C is a fit parameter that has to be estimated by comparing (3.1) with the common definition of the Reynolds number in a standard-viscosity run. Making use of this procedure, we obtain $C = 40$ and $Re = 9931$ for run A1 (table 1). Generalisation of the Reynolds number for systems with hyper-dissipation has been discussed by Spyksma, Magcalas & Campbell (2012).

Figure 2 displays the four MHD energy subfluxes, introduced in (2.6)–(2.7), and their sum. Also shown is $\mathcal{W}^\ell$, the resolved scale conversion of kinetic energy to magnetic energy (recall this does not represent energy transfer across ℓ). The two panels present fluxes obtained through different filters, results shown in figure 2(*a*) correspond to Galerkin truncation and those shown in figure 2(*a*) to the Gaussian filter of (2.12). The data shown in figure 2(*a*,*b*) are qualitatively similar but with quantitative differences. Focusing on the similarities, we see that the Inertial term $\langle \Pi^{I,\ell} \rangle$ is relatively weak and is the only one to exhibit inverse transfer regions, in the intervals $1.5 \times 10^2 \lesssim k\eta_\alpha \lesssim 2 \times 10^{-1}$ and

https://doi.org/10.1017/S0022377824000898 Published online by Cambridge University Press

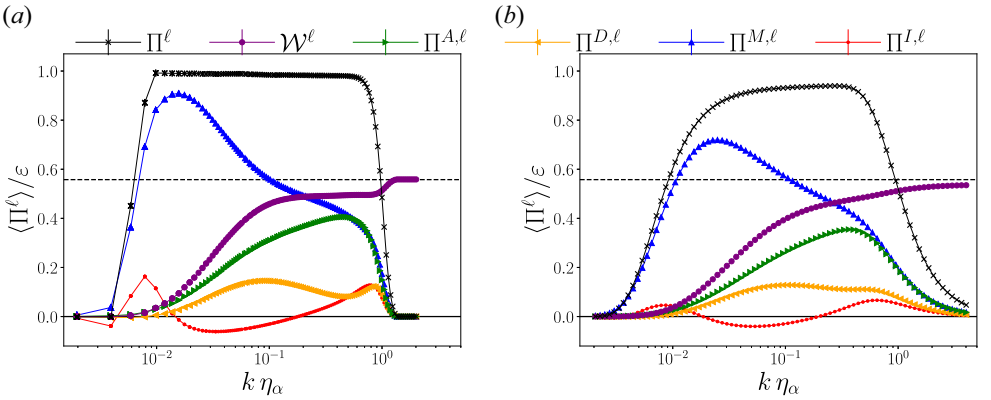

FIGURE 2. Terms contributing to the MHD filtered energy flux across scale ℓ, along with the resolved scale conversion (kinetic to magnetic) term, as a function of the adimensional parameter $k\eta_\alpha = \pi\eta_\alpha/\ell$: (*a*) Fourier filter; (*b*) Gaussian filter. All terms are normalised by the mean total energy dissipation rate $\varepsilon = \varepsilon_u + \varepsilon_b$. The dashed horizontal line indicates the normalised magnetic dissipation rate .. The error bars, although not fully visible, indicate one standard error. See (2.6)–(2.7).

$4 \times 10^{-3} \lesssim k\eta_\alpha \lesssim 6 \times 10^{-3}$. All the other subfluxes are associated with a direct cascade from the large to the small scales. The energy transfer from the momentum equation of (2.6) is almost entirely dominated by the Maxwell subflux ($-\Pi^{M,\ell}$) whose peak occurs in proximity to the forcing region. In contrast, the advection term from the induction equation ($\Pi^{A,\ell}$) is peaked at the small scales, close to the dissipative range. The conversion term, $\mathcal{W}^\ell$, is positive and increases monotonically with $k\eta_\alpha$. Particularly for the Fourier filter, it is roughly constant (i.e. scale independent) in the region $0.2 \lesssim k\eta_\alpha \lesssim 0.9$ where kinetic and magnetic subfluxes are in equipartition (Bian & Aluie 2019); see figure 11 in Appendix D. Also evident is a sudden increase of $\mathcal{W}^\ell$ in the dissipative range ($k\eta_\alpha \gtrsim 1$), due to hyperdiffusion, where the conversion rate saturates to ε_b as already pointed out by Bian & Aluie (2019).

Turning to the differences between the two kinds of filtering, we observe that the bandwidth of the inertial range plateau is narrower for the Gaussian filter case, roughly $k\eta_\alpha \in [0.04, 0.4]$ versus $k\eta_\alpha \in [0.012, 0.7]$. In general, the Gaussian filtering peaks are of lower amplitude and a little less localised. Linked to this is a more gradual roll-off of the fluxes at high $k\eta_\alpha$ and a slower convergence of $\mathcal{W}^\ell$ to ε_b with increasing k. These effects arise because Gaussian filtering at scale ℓ retains some effects from scales $\leq \ell$, unlike the situation for the sharp Galerkin truncation of the Fourier filter. For $\Pi^{D,\ell}$, there is also a qualitative difference, with the high-k local minimum and maximum seen with the Fourier filter essentially absent when the Gaussian filter is used.

4. Analysis and discussion

4.1. *Inertial flux and comparison with hydrodynamics*

The exact decomposition of the Inertial term $\Pi^{I,\ell}$, (2.8), is

$$\Pi^{I,\ell} = \Pi^{I,\ell}_{s,SSS} + \Pi^{I,\ell}_{m,SSS} + \Pi^{I,\ell}_{s,S\Omega\Omega} + \Pi^{I,\ell}_{m,S\Omega\Omega} + \Pi^{I,\ell}_{m,S\Omega S}, \tag{4.1}$$

where $\Pi^{I,\ell}_{s,S\Omega S}$ is not included as it is identically zero. This is the special case of (A3) where all the fields are the velocity and naturally it coincides with the original decomposition provided by Johnson (2020) for Navier–Stokes turbulence. It is thus of interest to

https://doi.org/10.1017/S0022377824000898 Published online by Cambridge University Press

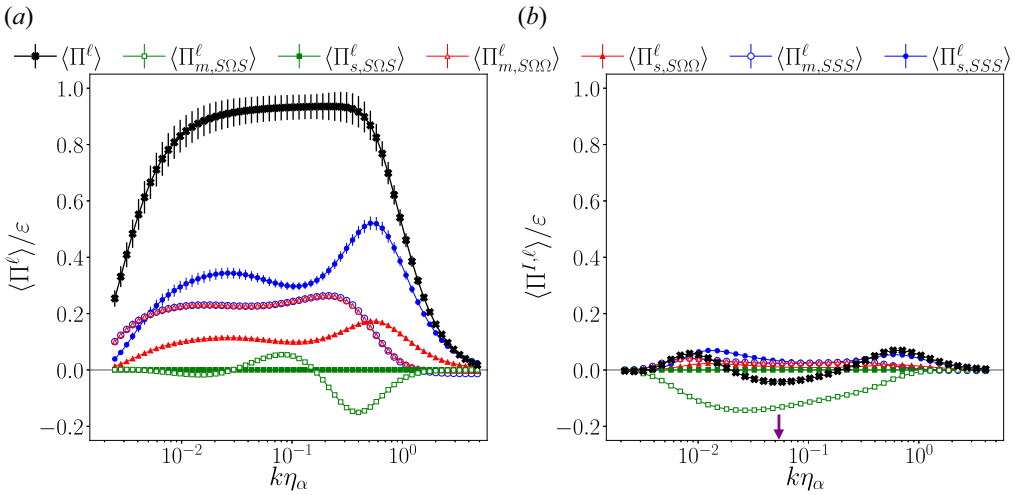

FIGURE 3. Contributions to the Inertial energy flux $\langle\Pi^{I,\ell}\rangle$ for (*a*) the HD dataset H2 and (*b*) the MHD dataset A1, as a function of the (non-dimensionalised) reciprocal scale ℓ, i.e. $\pi\eta_\alpha/\ell$. All fluxes are normalised by the mean total energy dissipation rate . for the dataset. Filled symbols correspond to single-scale contributions while hollow markers indicate multi-scale contributions. Error bars are for one standard error. Both panels indicate that $\langle\Pi^{I,\ell}_{m,SSS}\rangle \approx \langle\Pi^{I,\ell}_{m,S\Omega\Omega}\rangle$. In panel (*b*), the purple arrow locates $k\eta_\alpha = 5.4\times10^{-2}$ (equivalent to $kL_u \approx 14$), the value used for the probability density functions (p.d.f.s) shown in figures 4, 7 and 10.

investigate whether there are differences between the HD and MHD instances of (4.1), and how these might arise.

Figure 3 compares these two cases. For the hydrodynamic case, panel (*a*), there is a relatively clear and extended plateau for the total flux (and some of the subfluxes) corresponding to an inertial range. In contrast, the MHD case shown in panel (*b*) lacks such a plateau and the individual subfluxes are mostly much smaller than their hydrodynamic counterparts. Indeed, only $\langle\Pi^{I,\ell}_{m,SS\Omega}\rangle$ has values comparable to its hydrodynamic counterpart, albeit with a different functional form, being negative for almost all k. Intriguingly, this term is the only one that does not vanish point-wise in two-dimensional (2-D) turbulence, as discussed by Johnson (2021).[2] A depletion of the inertial flux in MHD turbulence has been observed by Alexakis (2013) and Yang *et al.* (2021) for configurations with large-scale electromagnetic forcing and by Offermans *et al.* (2018) for a saturated dynamo at lower Reynolds number. We have verified that the relation of Betchov (1956), $\langle\Pi^{I,\ell}_{s,SSS}\rangle = 3\langle\Pi^{I,\ell}_{s,S\Omega\Omega}\rangle$, holds for both datasets, as it must.

Also of interest is that there appears to be an approximate multi-scale analogue of the Betchov relation, with $\langle\Pi^{I,\ell}_{m,SSS} \approx \langle\Pi^{I,\ell}_{m,S\Omega\Omega}\rangle$. For hydrodynamics, this was already noted by Johnson (2021) and justified by Yang *et al.* (2023). Evidently, this approximate degeneracy also holds in this MHD situation, although the smallness of the terms makes this difficult to appreciate from figure 3(*b*).

Having discussed mean fluxes, we now examine some statistical properties of their pointwise contributions. Figure 4 presents standardised probability density functions (p.d.f.s) of the MHD Inertial subfluxes at $k\eta_\alpha = 5.4\times10^{-2}$. It is evident that the distributions are strongly non-Gaussian and exhibit very wide tails, with fluctuations at

[2]The energy flux decomposition for 2-D MHD turbulence is considered in Appendix C.

https://doi.org/10.1017/S0022377824000898 Published online by Cambridge University Press

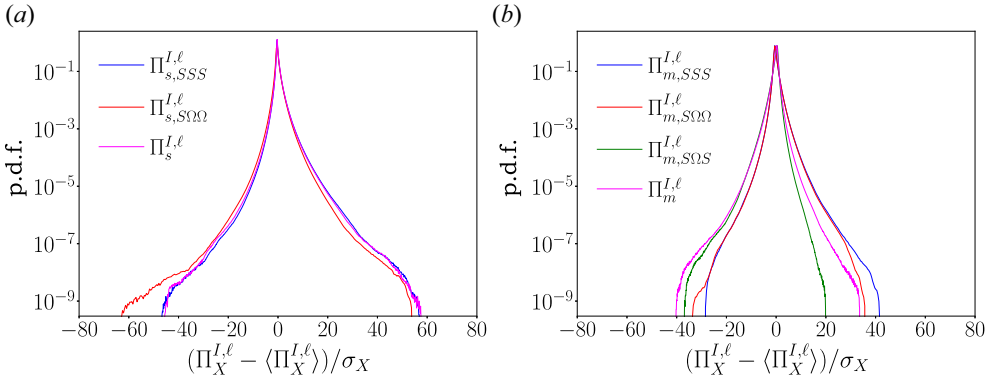

FIGURE 4. Standardised p.d.f.s of the MHD Inertial subfluxes $\Pi^{I,\ell}_X$ at $k\eta_\alpha = 5.4 \times 10^{-2}$ (equivalent to $kL_u = 14$) from dataset A1, where X identifies the specific subflux. (*a*) Single-scale fluxes; (*b*) multi-scale fluxes.

tens of standard deviations. (As we shall see, this is a common characteristic for all the MHD energy fluxes and subfluxes.) Most importantly, we observe strong backscatter in all subfluxes. That is, the depletion of the mean Inertial flux results from cancellations between forward and inverse transfer events made possible by an increase in backscatter events. Similar observations for the total Inertial term have been reported by Offermans *et al.* (2018), where a comparison between the kinematic, nonlinear and saturated stages of the dynamo had been carried out. The variance, skewness and kurtosis for each p.d.f. are reported in table 2. Although the p.d.f. of $\Pi^{I,\ell}_{s,S\Omega\Omega}$, which corresponds to the scale-local vortex stretching, has more asymmetrical tails than those of $\Pi^{I,\ell}_{s,SSS}$, the skewness for the latter is nonetheless larger. The term $\Pi^{I,\ell}_{s,S\Omega S}$ does not show up in figure 4 because it is identically zero due to the symmetries of the tensors involved in the corresponding trace of (A3). In contrast, panel (*b*) shows that . is the most negatively skewed p.d.f. among the Inertial ones.

In connection with the approximate degeneracy between $\Pi^{I,\ell}_{m,SSS}$ and $\Pi^{I,\ell}_{m,S\Omega\Omega}$ discussed above, figure 4(*b*) reveals that their p.d.f.s coincide up to events with a standardised probability density of 10^{-7}, potentially indicating that the approximate identity is true not just on average but also for higher-order moments, although further analysis is required.

4.2. *Maxwell flux*

The decomposition of the energy flux associated with the Lorentz force, which we refer to as the Maxwell term, $\Pi^{M,\ell}$ of (2.9), contains an extra (single-scale) term with respect to the Inertial flux. Specifically, from (A3), we obtain

$$\Pi^{M,\ell} = \Pi^{M,\ell}_{s,S\Sigma\Sigma} + \Pi^{M,\ell}_{m,S\Sigma\Sigma} + \Pi^{M,\ell}_{s,SJJ} + \Pi^{M,\ell}_{m,SJJ} + \Pi^{M,\ell}_{s,SJ\Sigma} + \Pi^{M,\ell}_{m,SJ\Sigma}. \tag{4.2}$$

Terms of type $S\Sigma\Sigma$ can be associated with strain rate amplification by magnetic shear, while terms of type SJJ correspond to current-filament stretching that is analogous to vortex stretching in HD. The last two terms are of type $SJ\Sigma$ and describe the back-reaction of the magnetic field on the flow or, more specifically, how the velocity strain rate is modified (typically amplified) in connection with a current-sheet thinning process. As we shall see, this is by far the dominant process. It proceeds as follows (figure 5). First, a current sheet is stretched by large-scale straining motions into a magnetic shear layer, in a process similar to vortex thinning in HD (Kraichnan 1976; Chen *et al.* 2006; Johnson

https://doi.org/10.1017/S0022377824000898 Published online by Cambridge University Press

	$\Pi_s^{I,\ell}$	$\Pi_{s,SSS}^{I,\ell}$	$\Pi_{s,S\Omega\Omega}^{I,\ell}$	$\Pi_m^{I,\ell}$	$\Pi_{m,SSS}^{I,\ell}$	$\Pi_{m,S\Omega S}^{I,\ell}$	$\Pi_{m,S\Omega\Omega}^{I,\ell}$	
$\left(\sigma_X^I\right)^2$	1.107	0.652	0.114	2.522	0.107	0.303	0.109	
S_X^I	2.958	3.234	1.483	.1.558	1.424	.2.155	1.301	
K_X^I	39.18	41.48	29.68	17.15	18.96	15.42	17.50	
	$\Pi_s^{M,\ell}$	$\Pi_{s,S\Sigma\Sigma}^{M,\ell}$	$\Pi_{s,SJJ}^{M,\ell}$	$\Pi_{s,SJ\Sigma}^{M,\ell}$	$\Pi_m^{M,\ell}$	$\Pi_{m,S\Sigma\Sigma}^{M,\ell}$	$\Pi_{m,SJ\Sigma}^{M,\ell}$	$\Pi_{m,SJJ}^{M,\ell}$
$\left(\sigma_X^M\right)^2$	0.112	0.014	0.0113	0.119	0.353	0.014	0.467	0.014
S_X^M	3.207	0.326	.0.827	4.030	3.105	.2.176	3.417	.2.289
K_X^M	32.22	32.71	31.09	39.88	21.34	27.96	24.60	28.46
	$\Pi_s^{A,\ell}$	$\Pi_{s,\Sigma\Sigma S}^{A,\ell}$	$\Pi_{s,\Sigma J\Omega}^{A,\ell}$	$\Pi_{s,\Sigma JS}^{A,\ell}$	$\Pi_{s,J\Sigma S}^{A,\ell}$	$\Pi_{s,JJS}^{A,\ell}$		
$\left(\sigma_X^A\right)^2$	0.206	0.014	0.004	0.030	0.030	0.011		
S_X^A	3.801	.0.333	.2.349	3.843	3.843	0.82		
K_X^A	42.16	32.71	53.12	38.90	39.90	31.08		
	$\Pi_m^{A,\ell}$	$\Pi_{m,\Sigma S\Sigma}^{A,\ell}$	$\Pi_{m,\Sigma\Sigma\Omega}^{A,\ell}$	$\Pi_{m,\Sigma J\Omega}^{A,\ell}$	$\Pi_{m,\Sigma JS}^{A,\ell}$	$\Pi_{m,J\Sigma S}^{A,\ell}$	$\Pi_{m,JJS}^{A,\ell}$	$\Pi_{m,J\Sigma\Omega}^{A,\ell}$	$\Pi_{m,JJ\Omega}^{A,\ell}$
$\left(\sigma_X^A\right)^2$	0.084	0.003	0.006	0.002	0.007	0.003	0.002	0.002	0.001
S_X^A	0.334	.1.616	.0.743	.2.011	.0.283	0.534	1.34	1.13	1.02
K_X^A	28.99	24.04	25.74	25.92	24.45	26.22	27.48	27.20	29.75
	$\Pi_s^{D,\ell}$	$\Pi_m^{D,\ell}$							
$\left(\sigma_X^D\right)^2$	0.039	0.055							
S_X^D	.1.918	1.804							
K_X^A	35.61	25.41							

TABLE 2. Values of variance $\left(\sigma_X^Y\right)^2$, skewness $S_X^Y = \left\langle \left(\Pi_X^{Y,\ell} - \langle \Pi_X^{Y,\ell} \rangle\right)^3 \right\rangle / \left(\sigma_X^Y\right)^3$ and kurtosis $K_X^Y = \left\langle \left(\Pi_X^{Y,\ell} - \langle \Pi_X^{Y,\ell} \rangle\right)^4 \right\rangle / \left(\sigma_X^Y\right)^4$ for the subflux p.d.f.s shown in figures 4–10, where X indicates the subflux identifier and Y denotes the term identifier.

2021). This results in a stretching of the magnetic flux tubes in the sheet. By conservation of magnetic flux, the magnetic field strength at the thereby generated smaller scales must increase. That is, magnetic energy is transferred from large to small scales. (We will revisit this process in § 4.3 in the context of the inter-scale transfer of magnetic energy.) The magnetic rate-of-strain field associated with the resulting magnetic shear layer now accelerates fluid along its extensional directions and slows it down in the compressional directions, thereby generating a stronger rate-of-strain field across smaller scales.

It is instructive to consider the process in two dimensions, in analogy to the vortex thinning of 2-D HD. In the reference frame of the rate-of-strain tensor at scale ℓ, the

https://doi.org/10.1017/S0022377824000898 Published online by Cambridge University Press

associated terms are

$$\Pi^{M,\ell}_{s,SJ\Sigma}(\boldsymbol{x}) = 2\lambda^{\ell}_{S}(\boldsymbol{x})\,\lambda^{\ell}_{\Sigma}(\boldsymbol{x})\,\bar{j}^{\ell}(\boldsymbol{x})\sin 2\psi(\boldsymbol{x}), \tag{4.3}$$

$$\Pi^{M,\ell}_{m,SJ\Sigma}(\boldsymbol{x}) = 2\int_{0}^{\ell^2} \mathrm{d}\theta \int_{\mathbb{R}^3} G^{\phi}(\boldsymbol{r})\,\lambda^{\ell}_{S}(\boldsymbol{x})\,\lambda^{\sqrt{\theta}}_{\Sigma}(\boldsymbol{x}+\boldsymbol{r})\,\bar{j}^{\sqrt{\theta}}(\boldsymbol{x}+\boldsymbol{r})\sin 2\psi(\boldsymbol{x}+\boldsymbol{r})\,\mathrm{d}\boldsymbol{r}, \tag{4.4}$$

where $\pm\lambda_S$ and $\pm\lambda_\Sigma$ are the eigenvalues of the velocity and magnetic rate-of-strain tensors, respectively, ψ the angle between the respective eigenvectors, and j the out-of-plane component of the current density. As can be seen from these formulae, a maximum energy transfer occurs when the principal axes of the magnetic rate-of strain tensor have a $\pm 45^{\circ}$ angle to those of the velocity rate-of-strain tensor. Depending on the sign of the out-of-plane current density and $\sin(2\psi)$, (4.3) and (4.4) result in a direct or an inverse energy transfer. Figure 5 presents a schematic depiction of the process. A direct energy transfer occurs if the angle between the principal axes of velocity and magnetic strain-rate tensors is in the same rotational direction as the out-of-plane current. A similar, albeit less straightforward, assessment is possible in three dimensions, where

$$\Pi^{M,\ell}_{s,SJ\Sigma}(\boldsymbol{x}) = 2\ell^2 \bar{S}^{\ell}_{ij}\bar{J}^{\ell}_{ik}\bar{\Sigma}^{\ell}_{kj} = 2\ell^2 \sum_{i=1}^{3}\sum_{j=1}^{3} \lambda^{\ell}_{i}\mu^{\ell}_{j}\cos^2\psi_{ij}, \tag{4.5}$$

and similarly for the multi-scale term. Here, μ^{ℓ}_{j} is the $j-$th eigenvalue of the symmetric part of the product matrix $\overline{J}^{\ell}_{ik}\overline{\Sigma}^{\ell}_{kj}$ (a contribution to the Maxwell SGS stress tensor) and ψ_{ij} the angle between the $i-$th eigenvector of $\bar{\mathbf{S}}^{\ell}$ and the $j-$th eigenvector of the symmetric part of $\overline{J}^{\ell}_{ik}\overline{\Sigma}^{\ell}_{kj}$. For a forward cascade of kinetic energy, $\langle\Pi^{M,\ell}\rangle > 0$, which implies that $\overline{S}^{\ell}_{ij}\overline{J}^{\ell}_{ik}\overline{\Sigma}^{\ell}_{kj}$ should be preferentially positive. Due to the presence of the cosine squared factor, this implies that the principal axes of the rate-of-strain tensor and those of the subscale stress must preferentially align, resulting in a stretching of the magnetic flux tubes along the extensional directions of the strain-rate tensor, as discussed above.

The subfluxes on the right-hand side of (4.2) and the total Maxwell flux are shown in figure 6, as a function of (non-dimensionalised) reciprocal ℓ. We see immediately that the net energy transfer proceeds from large scales to small scales with the total Maxwell flux $\langle\Pi^{M,\ell}\rangle$ being the dominant energy subflux for MHD, carrying approximately 80% of the total energy dissipation rate at its peak. At large scales, the major contribution is from the multi-scale term $\langle\Pi^{M,\ell}_{m,SJ\Sigma}\rangle$, switching to its single-scale partner, $\langle\Pi^{M,\ell}_{s,SJ\Sigma}\rangle$, as the dissipation scale is approached. All remaining terms in (4.2) are negligible. Summarising the mean Maxwell flux behaviour, we may say that the net kinetic energy transfer in MHD proceeds by the back-reaction of the magnetic field on the flow during the aforementioned current-sheet thinning process, while the contribution from current filament stretching and strain-amplification by magnetic shear are negligible.

The p.d.f.s for the Maxwell energy fluxes are shown in figure 7. The predominance of $\langle\Pi^{M,\ell}_{m,SJ\Sigma}\rangle$ in the direct cascade can be also appreciated by examining its p.d.f., which is the most positively skewed among the multi-scale terms of figure 7; see also table 2 for p.d.f. moments. As can be seen from the data shown in figure 7, while all terms of type $S\Sigma\Sigma$ and SJJ nearly vanish on average, fluctuations of approximately 60 standard deviations are not uncommon, and their multi-scale contributions show considerable backscatter. That is, the mean effects of current-filament stretching and strain-amplification by magnetic shear on the flow are negligible because of cancellations between pointwise forward and inverse transfers, and both these processes result in extreme backscatter events.

https://doi.org/10.1017/S0022377824000898 Published online by Cambridge University Press

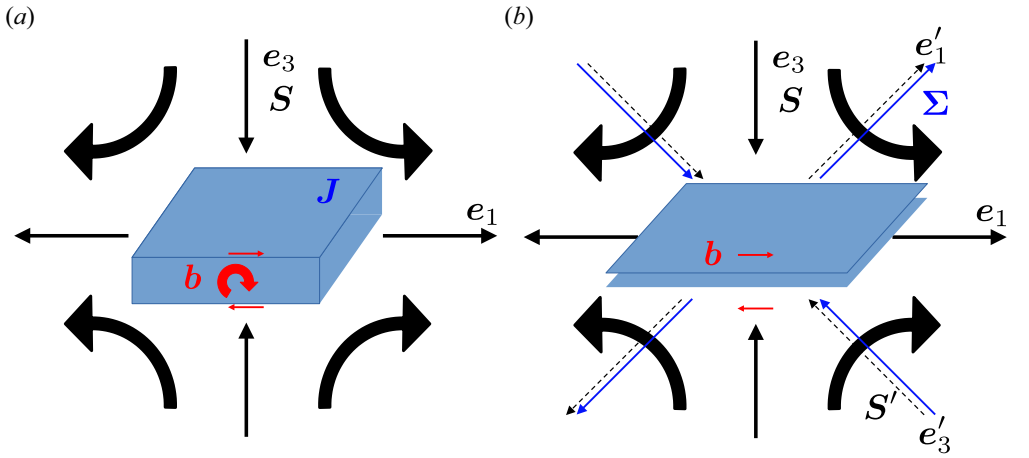

FIGURE 5. Two-dimensional sketch of current-sheet thinning and strain rate amplification by the latter. A current sheet, **J**, is stretched by (*a*) large-scale strain **S**, into a magnetic shear layer (**b**, red arrows). This induces a stretching of the magnetic flux tubes in the sheet. By conservation of magnetic flux, the magnetic field strength at the thereby generated smaller scales increases. That is, magnetic energy is transferred from large to small scales. The resulting magnetic shear layer has an associated magnetic strain rate field, Σ, whose principal axes (solid blue arrows) are at . to those of the large-scale strain rate tensor (straight black arrows). As the magnetic shear will align with the extensional direction of the (velocity) strain rate tensor, this causes the fluid to be accelerated along these extensional directions and slowed down in the compressional directions, thereby generating a stronger rate-of-strain field across smaller scales, **S**′, indicated by the dashed arrows. The principal axes of the large-scale strain rate tensor are denoted by $\mathbf{e}_1$ in one extensional direction and $\mathbf{e}_3$ in one compressional direction and analogously for the small-scale strain rate.

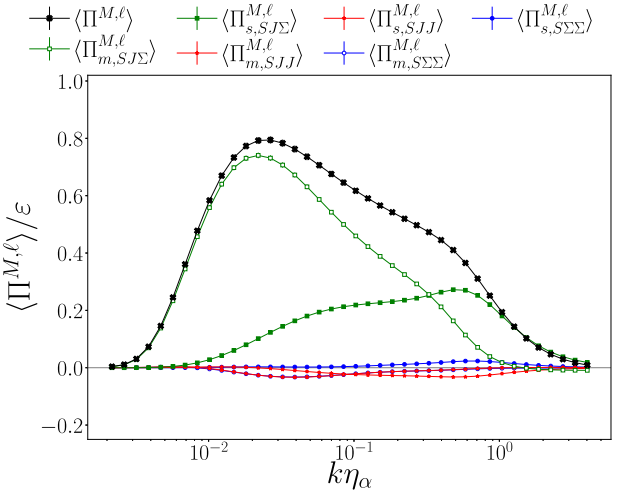

FIGURE 6. Contributions to the Maxwell energy flux .. Data are from dataset A1 and normalised by the mean total energy dissipation rate .. Error bars indicate one standard error.

https://doi.org/10.1017/S0022377824000898 Published online by Cambridge University Press

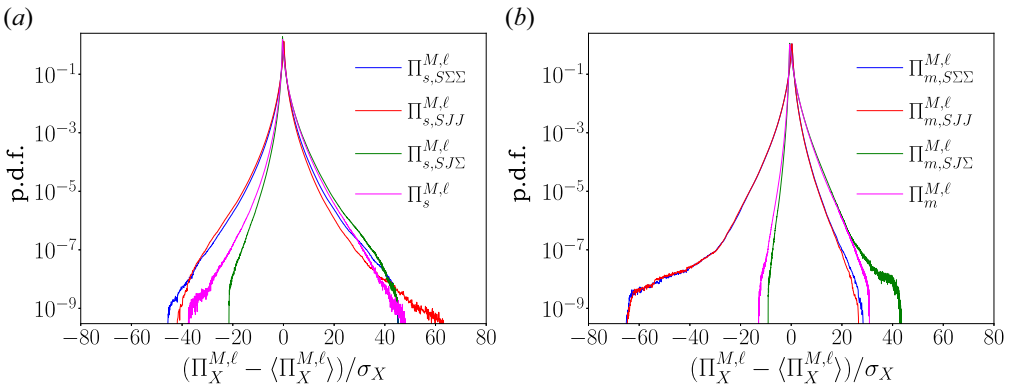

FIGURE 7. Standardised p.d.f.s for Maxwell subfluxes $\Pi_X^{M,\ell}$, at $k\eta_\alpha = 5.4 \times 10^{-2}$, from dataset A1, where X represents the subflux identifier. (*a*) Single-scale fluxes; (*b*) multi-scale fluxes. Note that the p.d.f.s for $\Pi_{m,S\Sigma\Sigma}^{M,\ell}$ and $\Pi_{m,SJJ}^{M,\ell}$ are approximately coincident.

In Appendix B, we show that the averages of the subfluxes $\Pi_{m,S\Sigma\Sigma}^{M,\ell}$ and $\Pi_{m,SJJ}^{M,\ell}$ can be connected via an exact Betchov-like relation that holds for all homogeneous flows,

$$\langle \Pi_{m,S\Sigma\Sigma}^{M,\ell} \rangle = \langle \Pi_{m,SJJ}^{M,\ell} \rangle + 2\langle \Pi_{m,\Omega\Sigma J}^{M,\ell} \rangle. \tag{4.6}$$

Note that the final term, $\Pi_{m,\Omega\Sigma J}^{M,\ell}$, does not appear in the Maxwell flux, (4.2), and our numerical results indicate $\Pi_{m,S\Sigma\Sigma}^{M,\ell} \approx \Pi_{m,SJJ}^{M,\ell}$, see figure 6. Physically, we may interpret this approximate identity as indicating that the net 'strain-production' by magnetic shear is almost equal to the net strain production by current-filament stretching. However, we stress again that these contributions to the interscale kinetic energy transfer are negligible. Further discussion on terms associated with strain production and current-filament stretching is provided in Appendix B.

4.3. *Advection and dynamo fluxes*

In this section, we focus on the decomposition of both the Advection term, $\Pi^{A,\ell}$, and the Dynamo term, $\Pi^{D,\ell}$, as defined in (2.10)–(2.11). As is well known, these two SGS fluxes share the same physical origin, namely the induced (fluctuation) electric field, and this is associated with certain symmetries and equivalences between the Advection and Dynamo subfluxes.

From the application of (A3), we find

$$\begin{aligned}\Pi^{A,\ell} = {} & \Pi_{s,\Sigma\Sigma S}^{A,\ell} + \Pi_{m,\Sigma\Sigma S}^{A,\ell} + \Pi_{m,\Sigma\Sigma\Omega}^{A,\ell} + \Pi_{s,\Sigma JS}^{A,\ell} + \Pi_{m,\Sigma JS}^{A,\ell} + \Pi_{s,\Sigma J\Omega}^{A,\ell} \\ & + \Pi_{m,\Sigma J\Omega}^{A,\ell} + \Pi_{s,J\Sigma S}^{A,\ell} + \Pi_{m,J\Sigma S}^{A,\ell} + \Pi_{s,J\Sigma\Omega}^{A,\ell} + \Pi_{m,J\Sigma\Omega}^{A,\ell} + \Pi_{s,JJS}^{A,\ell} + \Pi_{m,JJS}^{A,\ell} + \Pi_{m,JJ\Omega}^{A,\ell},\end{aligned} \tag{4.7}$$

$$\begin{aligned}\Pi^{D,\ell} = {} & \Pi_{s,\Sigma S\Sigma}^{D,\ell} + \Pi_{m,\Sigma S\Sigma}^{D,\ell} + \Pi_{s,\Sigma SJ}^{D,\ell} + \Pi_{m,\Sigma SJ}^{D,\ell} + \Pi_{m,\Sigma\Omega\Sigma}^{D,\ell} + \Pi_{s,\Sigma\Omega J}^{D,\ell} + \Pi_{m,\Sigma\Omega J}^{D,\ell} \\ & + \Pi_{s,JS\Sigma}^{D,\ell} + \Pi_{m,JS\Sigma}^{D,\ell} + \Pi_{s,JSJ}^{D,\ell} + \Pi_{m,JSJ}^{D,\ell} + \Pi_{s,J\Omega\Sigma}^{D,\ell} + \Pi_{m,J\Omega\Sigma}^{D,\ell} + \Pi_{m,J\Omega J}^{D,\ell},\end{aligned} \tag{4.8}$$

where we do not list terms that vanish identically, see Appendices A and F.

Figure 8 displays most of the Advection and Dynamo (sub)fluxes in separate panels. For clarity, only the subfluxes relevant to the discussion below and to the net energy flux are shown. The cyclic property of the trace can be used to show that some terms vanish

https://doi.org/10.1017/S0022377824000898 Published online by Cambridge University Press

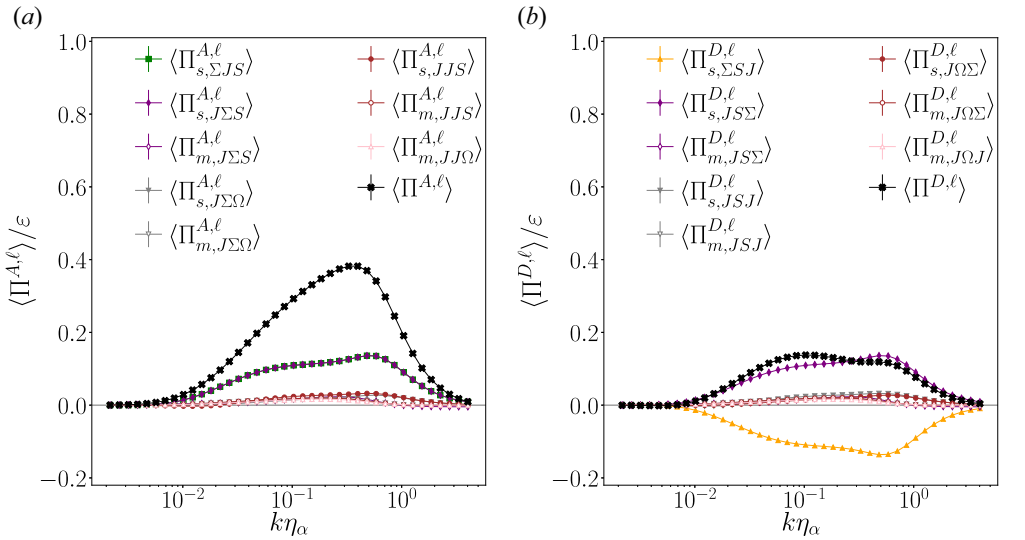

FIGURE 8. Decomposed fluxes for the (*a*) Advection term $\langle\Pi^{A,\ell}\rangle$ and (*b*) Dynamo term $\langle\Pi^{D,\ell}\rangle$. Fluxes are normalised by the mean total energy dissipation rate ε for dataset A1. In panel (*a*), $\langle\Pi^{A,\ell}_{s,\Sigma JS}\rangle$ and $\langle\Pi^{A,\ell}_{s,J\Sigma S}\rangle$ perfectly coincide. The error bars indicate one standard error.

identically and that each Advection subflux (both single-scale and multi-scale) is equal to (plus or minus) a partner Dynamo subflux; see the subfluxes expressions in Appendix F. For this reason, in figure 8, the following subflux pairs are not displayed since they are opposite in sign, $\Pi^{A,\ell}_{s,\Sigma\Sigma S}$ and $\Pi^{A,\ell}_{s,\Sigma S\Sigma}$ as well as $\Pi^{A,\ell}_{s,\Sigma J\Omega}$ and $\Pi^{A,\ell}_{s,\Sigma\Omega J}$ together with their multi-scale counterparts. Hence, these cancel pairwise and make no contribution to the net magnetic energy flux $\Pi^{A,\ell}+\Pi^{D,\ell}$; see Appendix F. In contrast, $\langle\Pi^{A,\ell}_{s,JJS}\rangle$ and $\Pi^{D,\ell}_{s,JSJ}$ and the related multi-scale terms, are equal and thus do contribute to the net flux.

Note, too, that the two Betchov relations (B6)–(B10) can provide another source of symmetry, or approximate symmetry.

The physical interpretation of the respective terms is very similar to what has been discussed for the Maxwell flux, except that now the effect of the flow on the magnetic field must be considered. Recall from § 4.2 that the Maxwell flux terms of type $SJ\Sigma$ correspond to the stretching and, by incompressibility, thinning of current sheets into magnetic shear layers, and that the back-reaction on the flow induced by this process is responsible for the bulk of the kinetic energy transfer to smaller scales. As we shall see, and as expected from the discussion of current-sheet thinning in § 4.2, this process also transfers most magnetic energy from large to small scales. However, in contrast to the Maxwell flux situation (dominated by a multi-scale term), here it is two of the Advection single-scale terms, ΣJS and $J\Sigma S$, that carry most of the magnetic energy flux.

Focusing on the Advection term, from figure 8(*a*), we observe that the net flux is everywhere positive and peaked at smaller scales, roughly at the end of the inertial range. Recall that the Maxwell flux is peaked at larger scales (figure 6). Due to the cyclic property of the trace, the terms $\Pi^{A,\ell}_{s,\Sigma JS}$ and $\Pi^{A,\ell}_{s,J\Sigma S}$ are equal while, because of the symmetry of the tensors involved, the subfluxes $\Pi^{A,\ell}_{s,JJ\Omega}$ and $\Pi^{A,\ell}_{s,\Sigma\Sigma\Omega}$ together with $\Pi^{D,\ell}_{s,J\Omega J}$ and $\Pi^{D,\ell}_{s,\Sigma\Omega\Sigma}$ are identically zero. It is also apparent from figure 8(*a*) that the remaining Advection terms make negligible contributions to the net flux. We note that $\Sigma\Sigma S$ type terms correspond to magnetic shear amplification due to straining motions and those

https://doi.org/10.1017/S0022377824000898 Published online by Cambridge University Press

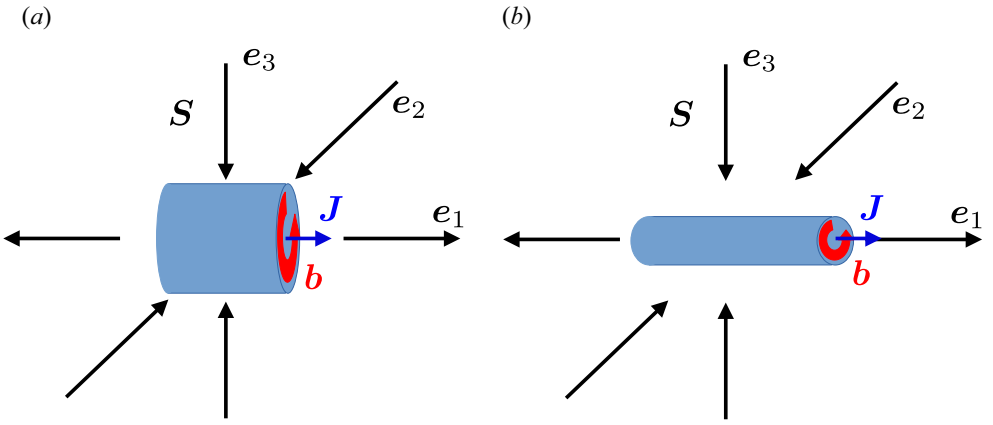

FIGURE 9. Sketch of current-filament stretching. A current filament **J**, with associated magnetic field **b**, is (*a*) stretched by large-scale strain, **S** with two contractional and one extensional direction into (*b*) a longer and thinner filament along the extensional direction. This induces a stretching of the magnetic flux tubes in the filament. By conservation of magnetic flux, the magnetic field strength at the thereby generated smaller scales increases (red arrows). That is, magnetic energy is transferred from large to small scales. This process is analogous to vortex stretching in hydrodynamic turbulence. The principal axes of the large-scale strain rate tensor are denoted by $\mathbf{e}_1$ in the extensional direction and $\mathbf{e}_2$ and $\mathbf{e}_3$ in the contractional directions.

of type *JJS* to current filament stretching – the analogue to vortex stretching in HD – as depicted in figure 9. Terms of type $\Sigma J\Omega$ encode bending of magnetic field lines into current filaments by rotational flow, i.e. a change in the magnetic-field geometry induced by vortical motion. Thus, the net Advection term is primarily due to single-scale contributions, being approximately equal to $2\,\Pi^{A,\ell}_{s,\Sigma JS}$, and it carries approximately 40% of the total energy flux at its peak.

For the Dynamo term, $\Pi^{D,\ell}$, we observe that the net flux is almost flat in the inertial range, substantially positive definite for these scales (figure 8*b*) and responsible for approximately 15% of the total energy flux. All subfluxes, except $\Pi^{D,\ell}_{s,\Sigma SJ}$ shown in yellow and $\Pi^{D,\ell}_{s,JS\Sigma}$ indicated by the filled purple symbols, are negligible. However, using the cyclic property once again, one can show that $\Pi^{D,\ell}_{s,\Sigma SJ} = -\Pi^{D,\ell}_{s,JS\Sigma}$; hence, these two terms cancel out and do not contribute to the net flux. In contrast to the Advection term, the major contributions to the net Dynamo term are from subleading single and multi-scale subfluxes of various types, with each contributing only 1–2 % to the total energy flux adding up to a total of approximately 15% of the total energy flux. In summary, single-scale current-sheet thinning is the dominant process transferring magnetic energy across scales. It solely originates from the advective term in the induction equation.

Consider now the p.d.f.s. As a consequence of the symmetries between Dynamo and Advection subfluxes, only the Advection p.d.f.s are shown in figures 10(*a*) and 10(*c*), respectively for the single-scale terms and the multi-scale terms. It is striking that the p.d.f. of $\Pi^{A,\ell}_{s,\Sigma J\Omega}$, which describes the bending of magnetic field lines into current filaments by rotational flow, is by far the most strongly fluctuating with huge fluctuations of more than 100 standard deviations, also showing strong magnetic backscatter. In contrast, the aforementioned current-sheet thinning process, that is mostly responsible for the forward cascade of magnetic energy, shows weak magnetic backscatter. The other Advection subflux p.d.f.s, both single-scale and multi-scale, span a range comparable

https://doi.org/10.1017/S0022377824000898 Published online by Cambridge University Press

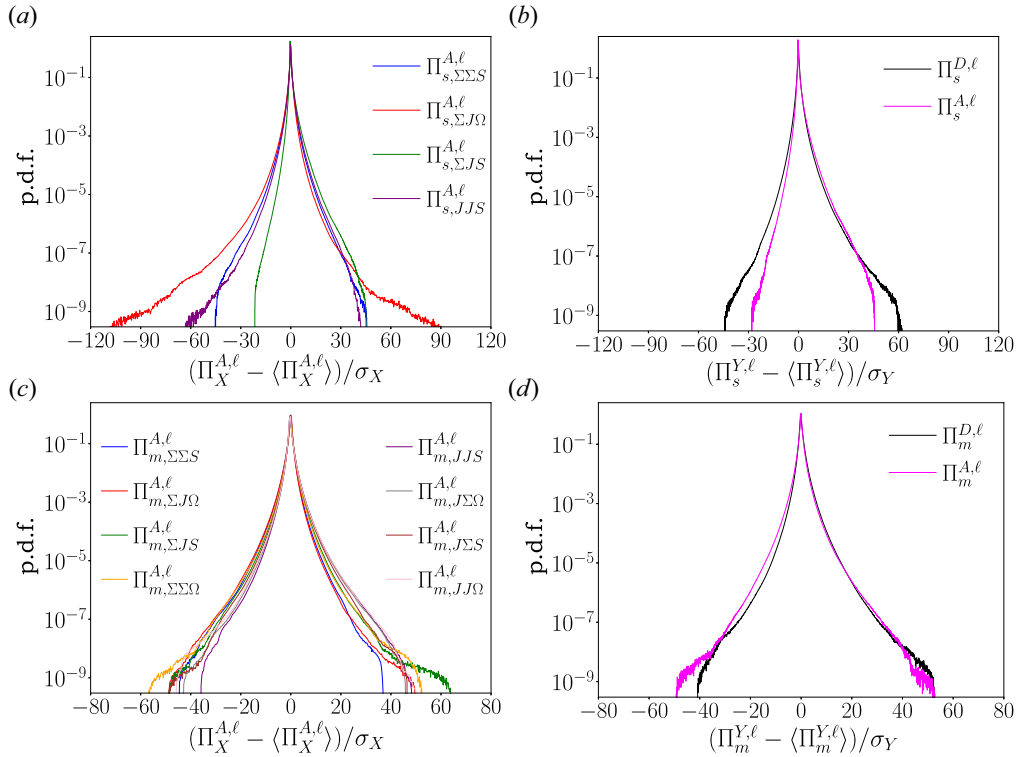

FIGURE 10. Standardised p.d.f.s for dataset A1 at $k\eta_\alpha = 5.4 \times 10^{-2}$. (*a*) Single-scale Advection subfluxes $\Pi^{A,\ell}_X$, where X represents the subflux identifier, and (*b*) net single-scale fluxes for the Dynamo ($\Pi^{D,\ell}_s$) and Advection terms ($\Pi^{A,\ell}_s$). In the x-axis titles for panels (*b*) and (*d*), $Y = A$ or D, as appropriate. Note that $\Pi^{A,\ell}_{s,\Sigma JS} = \Pi^{A,\ell}_{s,JS\Sigma}$ (see figure 8). (*c*,*d*) As for panels (*a*,*b*) except for the multi-scale subfluxes of $\Pi^{A,\ell}$ and $\Pi^{D,\ell}$. Note that panels (*c*,*d*) have the same x-axis range as figures 4 and 7.

with those associated with the p.d.f.s for the Inertial and Maxwell fluxes. Moreover, all the multi-scale fluxes (Advection and Dynamo) have quite similar p.d.f.s, and thus so do the net multi-scale flux p.d.f.s (figure 10*d*). In the case of the net single-scale p.d.f.s, the Advection–Dynamo agreement is still good in the cores of the distributions, but there is a significant difference at larger negative fluctuations (figure 10*b*).

4.4. *Total energy flux, .*

In the preceding subsections, we analysed the four contributions to the incompressible MHD energy flux, finding that each of them may be reasonably well approximated using just some of the subfluxes. These approximations may now be assembled to give an approximate form for the mean total MHD energy flux. Specifically, we suggest that

$$\left\langle \Pi^\ell \right\rangle = \left\langle \Pi^{I,\ell} \right\rangle + \left\langle \Pi^{M,\ell} \right\rangle + \left\langle \Pi^{A,\ell} \right\rangle + \left\langle \Pi^{D,\ell} \right\rangle \approx -2\langle \Pi^{M,\ell}_{s,SJ\Sigma} \rangle - \langle \Pi^{M,\ell}_{m,SJ\Sigma} \rangle \tag{4.9}$$

$$= 4\ell^2 \left\langle \mathrm{Tr}\left\{ (\bar{\boldsymbol{S}}^\ell)^t \bar{\boldsymbol{J}}^\ell (\bar{\boldsymbol{\Sigma}}^\ell)^t \right\} \right\rangle \tag{4.10}$$

$$+ 2\left\langle \int_0^{\ell^2} \mathrm{d}\theta\, \mathrm{Tr}\left\{ (\bar{\boldsymbol{S}}^\ell)^t \left(\overline{\bar{\boldsymbol{J}}^{\sqrt{\theta}} \left(\bar{\boldsymbol{\Sigma}}^{\sqrt{\theta}} \right)^t}^{\phi} - \overline{\bar{\boldsymbol{J}}^{\sqrt{\theta}}}^{\phi} \overline{\left(\bar{\boldsymbol{\Sigma}}^{\sqrt{\theta}} \right)^t}^{\phi} \right) \right\} \right\rangle \tag{4.11}$$

https://doi.org/10.1017/S0022377824000898 Published online by Cambridge University Press

is a suitable expression. Note that, after using cyclic properties of the trace, this is expressed only in terms of two of the Maxwell subfluxes, one single-scale and one multi-scale. These are discussed in § 4.2 and we remind the reader that all subflux definitions can be found in Appendix F. Interestingly, the terms on the right-hand side of (4.11) are part of a group of terms that remain non-zero in 2-D MHD; see Appendix C. We intend to explore this intriguing feature in future work.

Equation (4.11) demonstrates that the mean total energy flux in MHD turbulence is largely given by the stretching and thinning of current-sheets into magnetic shear layers by large-scale strain, resulting in a transfer of magnetic energy from large to small scales. In addition, there is a back-reaction of this process on the flow, whereby the ensuing magnetic strain-rate field accelerates fluid along its extensional directions and slows it down in the compressional directions, thereby generating a stronger strain-rate field across smaller scales, as shown schematically in figure 5.

4.5. *Current-sheet thinning and magnetic reconnection*

As a means of inter-scale energy transfer, the current-sheet thinning process can only proceed as described in an inertial range, i.e. at scales where Joule and viscous dissipation are negligible. As the dissipative scales are approached, Alfvén's theorem ceases to hold and magnetic reconnection can occur, with associated changes to the topology of the magnetic field. Interestingly, models of MHD reconnection are geometrically very similar to the inertial-range energy transfer process described here. For example in the Sweet–Parker model (Parker 1957; Sweet 1958), a current sheet is thinned by a flow that pushes magnetic field lines closer and closer together. Eventually, when the distance between the field lines approaches scales where Joule dissipation becomes important, the topological conservation of the magnetic field is broken and magnetic field-lines reconnect. That is, the continuation of the current-sheet thinning process described herein, and shown conceptually in figure 5, to smaller and smaller scales can lead naturally to magnetic reconnection.

5. Consequences for MHD subgrid-scale modelling

MHD LES modelling usually proceeds through variations on the Clark and Smagorinsky models, here shown for simplicity for the HD case,

$$\tau_{ij}^{\mathrm{CLARK}} = \ell^2 \partial_k \bar{u}_i^\ell \partial_k \bar{u}_j^\ell \tag{5.1}$$

for the Clark model (Clark *et al.* 1979; Pope 2000),[3] where we note that this model corresponds to what we have herein called single-scale flux contributions (see the first term on the right-hand side of (2.15)), and the Smagorinsky model

$$\tau_{ij}^{\mathrm{SMAG}} = -2\nu_e \bar{S}_{ij}^\ell, \tag{5.2}$$

where . is the turbulent or eddy viscosity given by

$$\nu_e = (C_S \ell)^2 \sqrt{\bar{S}_{ij}^\ell \bar{S}_{ij}^\ell}, \tag{5.3}$$

with . being a free parameter, the Smagorinsky constant (Smagorinsky 1963). This is the case for incompressible MHD (Zhou & Vahala 1991; Müller & Carati 2002; Kessar *et al.* 2016). Moreover, adaptations have been made for the compressible case (Chernyshov,

[3]The factor 1/12 that figures in the original definition of the Clark model has here been absorbed in the filter scale ℓ^2.

https://doi.org/10.1017/S0022377824000898 Published online by Cambridge University Press

Karelsky & Petrosyan 2010; Grete *et al.* 2016; Vlaykov *et al.* 2016), for channel flow at high magnetic Reynolds number (Hamba & Tsuchiya 2010; Jadhav & Chandy 2021, 2023) and for extensions of MHD taking various levels of microphysics terms into account, such as Hall MHD (Miura, Araki & Hamba 2016) or Braginskii-extended (two-fluid) MHD (Miura, Hamba & Ito 2017), with the latter specifically focussed on the ballooning instability in stellarator devices. Most such approaches use the same SGS model for the inertial and Maxwell stresses based on velocity-field gradients with eddy viscosities involving either only the strain rate tensor or a weighted sum of the squared strain rate and the squared current, and similarly structured SGS models for the induction equation, with either heuristics or trial-and-error approaches to find suitable values for model constants. In what follows, we briefly discuss how the present results can be used to construct suitably structured SGS models for each SGS-stress in the MHD equations.

In terms of SGS modelling, our simulation-based results suggest that the Inertial terms can be neglected and a dissipative model, such as the Smagorinsky model, for the Maxwell stresses should suffice to capture the (leading-order) mean effects. In terms of fluctuations, we find that the observed mean Inertial flux depletion is caused by considerable backscatter in all Inertial subfluxes (see figure 4). This could suggest that a more sophisticated model would be required for the Inertial term. However, in 3-D HD turbulence, backscatter-free SGS models such as the standard static Smagorinsky closure perform well in capturing high-order statistics, that is, anomalous exponents and multifractal predictions for the correlation between velocity-field increments and SGS stresses (Linkmann, Buzzicotti & Biferale 2018). Furthermore, as the SGS stresses enter the filtered Navier–Stokes equation only through their divergence, this results in a degree of (gauge) freedom to determine model stress tensors that produce much less backscatter than those constructed using the standard definition (Vela-Martín 2022). In fact, backscatter can be traced back to spatial fluxes disconnected from the (scale-space) energy transfer and as such does not require modelling (Vela-Martín 2022).

For the magnetic energy transfers, we observe the net transfers are from large to small scales, suggesting again that dissipative models should suffice. Indeed, as multi-scale terms in our flux decomposition are negligible, a Clark-type model involving only the coupling between current and strain-rate tensors may work well for a nonlinear saturated non-helical (small-scale) dynamo. However, additional stabilising terms may be required as the Clark (or gradient) model is know to result in numerically unstable LES of a mixing layer in HD (Vreman, Geurts & Kuerten 1996, 1997) and for MHD (Müller & Carati 2002; Kessar *et al.* 2016), as discussed in further detail below. Similar to the Inertial term results, we observe considerable backscatter in the magnetic energy fluxes (see figure 10), and it remains to be seen if the aforementioned results by Linkmann *et al.* (2018) on the effect of SGS closures on high-order statistics carry over from HD to MHD.

For a non-helical saturated dynamo, as is the case here, Müller & Carati (2002) and Kessar *et al.* (2016) carried out MHD LES with Clark-type models constructed from the full velocity and magnetic-field gradients for the sum of the Reynolds and Maxwell SGS stress in the momentum equation and for the magnetic stresses, resulting in unstable simulations as in the HD case. Using *a priori* analyses of DNS data, Kessar *et al.* (2016) trace the instabilities back to the Clark terms transferring an insufficient amount of kinetic and magnetic energy to small scales, and to a production of backscatter. According to our analysis, for the momentum equation, the former effect is due to the Maxwell stress having a significant multi-scale component which is not captured in the Clark model. Concerning the latter, we also observe strong backscatter from the kinetic and magnetic single-scale subfluxes except for terms connected with current-sheet thinning, see figures 4, 7 and 10. Furthermore, a Clark model based on the full gradients by generalisation of (5.1) to MHD

https://doi.org/10.1017/S0022377824000898 Published online by Cambridge University Press

will introduce effects that are not present in the full MHD dynamics especially concerning the Maxwell and magnetic stresses, as all combinations of vorticity, strain, current and magnetic strain are included in the model and equally weighted,

$$\tau_{ij}^{\mathrm{CLARK},M} = \ell^2 \partial_k \bar{b}_i^\ell \partial_k \bar{b}_j^\ell = \ell^2 \left(\bar{\Sigma}_{ik}^\ell \bar{\Sigma}_{jk}^\ell + \bar{\Sigma}_{ik}^\ell \bar{J}_{jk}^\ell + \bar{J}_{ik}^\ell \bar{\Sigma}_{jk}^\ell + \bar{J}_{ik}^\ell \bar{J}_{jk}^\ell \right), \tag{5.4}$$

$$\tau_{ij}^{\mathrm{CLARK},A} = \ell^2 \partial_k \bar{b}_i^\ell \partial_k \bar{u}_j^\ell = \ell^2 \left(\bar{\Sigma}_{ik}^\ell \bar{S}_{jk}^\ell + \bar{J}_{ik}^\ell \bar{S}_{jk}^\ell + \bar{\Sigma}_{ik}^\ell \bar{\Omega}_{jk}^\ell + \bar{J}_{ik}^\ell \bar{\Omega}_{jk}^\ell \right), \tag{5.5}$$

$$\tau_{ij}^{\mathrm{CLARK},D} = \ell^2 \partial_k \bar{u}_i^\ell \partial_k \bar{b}_j^\ell = \ell^2 \left(\bar{S}_{ik}^\ell \bar{\Sigma}_{jk}^\ell + \bar{\Omega}_{ik}^\ell \bar{\Sigma}_{jk}^\ell + \bar{S}_{ik}^\ell \bar{J}_{jk}^\ell + \bar{\Omega}_{ik}^\ell \bar{J}_{jk}^\ell \right). \tag{5.6}$$

Our analysis, however, shows that only terms stemming from the coupling between current and strain-rate tensors are significant, with all remaining contributions to the net Maxwell and magnetic fluxes being negligible. Thus, retaining these contributions in an SGS model may substantially (and inappropriately) affect the small-scale structure of the flow and the magnetic field, and lead to an overestimation of backscatter. It remains to be seen if backscatter-related instabilities can be suppressed if only the current-sheet thinning (CST) terms,

$$\tau_{ij}^{\mathrm{CST},M} = \ell^2 \left(\bar{\Sigma}_{ik}^\ell \bar{J}_{jk}^\ell + \bar{J}_{ik}^\ell \bar{\Sigma}_{jk}^\ell \right), \tag{5.7}$$

$$\tau_{ij}^{\mathrm{CST},A} = \ell^2 \left(\bar{\Sigma}_{ik}^\ell \bar{S}_{jk}^\ell + \bar{J}_{ik}^\ell \bar{S}_{jk}^\ell \right), \tag{5.8}$$

$$\tau_{ij}^{\mathrm{CST},D} = \ell^2 \left(\bar{S}_{ik}^\ell \bar{\Sigma}_{jk}^\ell + \bar{S}_{ik}^\ell \bar{J}_{jk}^\ell \right), \tag{5.9}$$

are retained. That is, both magnetic strain and current density tensors must be included in SGS models as recently discussed by Alexakis & Chibbaro (2022).

A further challenge for LES modelling of MHD turbulence is to accurately capture the transfer of magnetic to kinetic energy (Haugen & Brandenburg 2006) and *vice versa*. Using standard Smagorinsky models for both the momentum and induction equations, Haugen & Brandenburg (2006) showed that the Smagorinsky constant can be fine-tuned to obtain a good agreement between filtered DNS and LES for kinetic energy spectra, but only at the expense of a strong suppression of the (nonlinear) dynamo. Moreover, as discussed by Offermans *et al.* (2018), the resolved-scale conversion term must either be fully accounted for in LES, resulting in the need to resolve all scales where this term is active, or in the present case of a saturated dynamo, a model including an extra term accounting for the under-resolved dynamo effect must be provided.

In this paper, we have only considered the no mean magnetic field situation. The presence of a strong background magnetic field is likely to require an SGS modelling approach that differs from those just discussed, as the ensuing anisotropy and two-dimensionalisation of magnetic- and velocity-field fluctuations may result in partial inverse fluxes. We will report results on configurations with strong background magnetic fields in due course. Similarly, the large-scale (helical) dynamo requires an investigation in its own right, and the magnetic-field growth at large scales is likely to require a different type of SGS modelling approach, as Kessar *et al.* (2016) report that the Clark and even a standard static Smagorinsky model result in unstable LES.

The method discussed here can be readily extended to Hall and two-fluid MHD and other fluid models for plasma turbulence. For instance, the applicability of the Smagorinsky closure to Hall MHD has been assessed by an *a priori* analysis using sharp filtering (Miura & Araki 2012) prior to the deployment of said closure (Miura *et al.* 2016). An *a priori* analysis and decomposition of the Hall flux in analogy to the results presented here could lead to a better understanding of the physics of the interscale magnetic energy transfer induced by the Hall effect and thus to a refinement of Hall-MHD SGS models.

https://doi.org/10.1017/S0022377824000898 Published online by Cambridge University Press

Finally, we point out that a new LES method, so-called physics-inspired coarsening (PIC), has been devised recently (Johnson 2022). In the homogeneous case, this approach reduces to Gaussian filtering and the representation of SGS stresses in terms of field gradients as generalised herein. In PIC, the velocity field advanced in LES is formally obtained by artificial viscous smoothing, with the required pseudo-diffusion being introduced through an auxiliary Stokes equation. This approach may be generalisable to MHD and more complex fluid models applicable to plasma turbulence.

6. Conclusions

Generalising a method introduced by Johnson (2020) for Navier–Stokes turbulence, we have presented a general analytical method for obtaining exact forms for inter-scale fluxes in advection–diffusion equations through products of vector-field gradients, and applied it to kinetic and magnetic energy fluxes in homogeneous MHD turbulence. The aim was to provide expressions for subfluxes that are physically interpretable in terms of the action of the magnetic field on the flow and *vice versa*. A quantification thereof is of interest for the fundamental understanding of cascade processes in MHD turbulence, and also provides guidance as to what physics needs to be captured in subgrid-scale models and how such models should be constructed so that they preserve, at least approximately, empirical features of the mean energy fluxes and their fluctuations.

In MHD, scale-space energy fluxes are defined as the contraction of velocity- or magnetic-field gradients with the appropriate subgrid-scale stresses. Rewriting these in terms of symmetric and antisymmetric components of field-gradients tensors yields terms with clear physical meanings. For example, strain and vorticity in the case of the velocity field, and current and magnetic strain/shear for the magnetic field. Expressing the MHD SGS stresses in terms of vorticity, rate-of-strain, current and magnetic rate-of-strain results in an exact decomposition of magnetic and kinetic energy fluxes in terms of interactions between the symmetric and antisymmetric components of velocity- and magnetic-field gradients.

The kinetic energy flux comprises two terms, the Inertial flux (as in hydrodynamics) and a flux term associated with the action of the Lorentz force on the flow. The former is decomposed into terms associated with vortex stretching, strain self-amplification and strain-vorticity alignment. A term-by-term comparison between the Inertial fluxes in HD and MHD turbulence shows that all Inertial subfluxes are depleted due to cancellations between forward scatter and backscatter events, and are indeed almost negligible in MHD turbulence. That is, the physics of the kinetic energy cascade is very different in statistically steady MHD turbulence as compared with HD turbulence, as vortex stretching and strain self-amplification have, on average, very little effect. In MHD turbulence, almost all kinetic energy is transferred downscale by a current-sheet thinning process: in regions of large strain, current sheets are stretched by large-scale straining motion into regions of magnetic shear. This magnetic shear in turn drives extensional flows at smaller scales. The magnetic energy is mainly transferred from large to small scales by the aforementioned current-sheet thinning in regions of high strain, while the mean contributions from current-filament stretching – the analogue to vortex stretching – and bending of magnetic field lines in high magnetic strain regions into current filament by vortical motion are almost negligible. The latter effect, which results in a change in the magnetic field geometry at small scales is associated with strong magnetic backscatter. A decomposition into single- and multi-scale components of the subfluxes shows that the mean kinetic energy flux induced by the back-reaction of current-sheet thinning on the flow has a strong multi-scale component especially at large scales where the magnetic field is weak, while the multi-scale component of the magnetic energy flux is almost

https://doi.org/10.1017/S0022377824000898 Published online by Cambridge University Press

negligible. We consistently observe that the multi-scale components of the respective flux terms fluctuate less than the single-scale components.

Finally, we note that the method can be further expanded in various directions. Within MHD turbulence, for instance, decompositions of the magnetic helicity and cross-helicity fluxes could identify the physics driving these respective cascades with potential implication for selective decay for decaying MHD turbulence. Kinetic energy transfer across scales and its conversion to magnetic energy, and *vice versa*, depend on the value of the magnetic Prandtl number (Brandenburg & Rempel 2019). The methodology introduced here could be used to quantify the .-dependence of the different physical processes involved in the energy cascade. Another possibility would be to include temperature fluctuations. An extension or application to compressible flows would be of interest especially for astrophysical plasmas. As flux terms associated with any advective nonlinearity can be analysed by this method, a decomposition of Hall MHD and of fluid models of ion- or electron-temperature-gradient turbulence (Ivanov *et al.* 2020; Adkins *et al.* 2022; Ivanov, Schekochihin & Dorland 2022) may be of interest for the magnetic confinement fusion community.

Acknowledgements

Editor S. Tobias thanks the referees for their advice in evaluating this article.

Funding

This work used the ARCHER2 UK National Supercomputing Service (https://www.archer2.ac.uk) with resources provided by the UK Turbulence Consortium (EPSRC grants EP/R029326/1 and EP/X035484/1) and received funding from the European Research Council (ERC) under the European Union's Horizon 2020 research and innovation programme (grant agreement No 882340, L. Biferale).

Declaration of interests

The authors report no conflict of interest.

Appendix A. General formulation of advective-type SGS flux terms

In § 2.3, we derived, following Johnson (2020, 2021), the form for the scale-filtered magnetic energy flux associated with the $\mathbf{u}\cdot\nabla\mathbf{b}$ term of the induction equation. Here, we outline how this approach is generally applicable for flux terms involving three distinct fields, connected with an (unfiltered) term of the form $\mathbf{x}\cdot(\mathbf{z}\cdot\nabla)\,\mathbf{y}$, where $\mathbf{x}$, $\mathbf{y}$ and $\mathbf{z}$ are solenoidal, but otherwise arbitrary, 3-D vector fields (they are not coordinate vectors). For appropriate mappings of $\mathbf{x}$, $\mathbf{y}$, $\mathbf{z}$ to $\mathbf{u}$ and $\mathbf{b}$, this will yield any of the desired MHD SGS energy fluxes, (2.8)–(2.11). Moreover, the SGS fluxes associated with helically decomposed hydrodynamics and MHD (Waleffe 1993; Lessinnes *et al.* 2011; Linkmann *et al.* 2015; Alexakis 2017; Alexakis & Biferale 2018; Yang *et al.* 2021) and the kinetic, magnetic and cross-helicities may be obtained using similar special cases, see Capocci *et al.* (2023) for a decomposition of the kinetic helicity flux in Navier–Stokes turbulence.

The SGS stresses at scale ℓ associated with $\mathbf{z}\cdot\nabla\mathbf{y}$ are

$$\tau^{\ell}(y_i, z_j) = \overline{y_i z_j}^{\ell} - \overline{y_i}^{\ell}\,\overline{z_j}^{\ell}, \tag{A1}$$

where the choice of the filter kernel is for now arbitrary. Clearly, $\left(\tau^{\ell}(y_i, z_j)\right)^t = \tau^{\ell}\left(z_i, y_j\right)$, where $(\cdot)^t$ denotes matrix transpose. Note that the advecting field is $\mathbf{z}$. Contracting the SGS stress against the gradient tensor of a third arbitrary field, $\mathbf{x}$, yields the general SGS

https://doi.org/10.1017/S0022377824000898 Published online by Cambridge University Press

flux term

$$\Pi^{\ell}_{xyz} = -\left(\partial_j \bar{x}^{\ell}_i\right) \tau^{\ell}(y_i, z_j). \tag{A2}$$

Here, we have included a leading minus sign in (A2). However, if one wishes to have $\Pi^{\ell}_{xyz} > 0$ always correspond to forward transfer – as we have elected to do herein – this may not be correct. It depends on the sign the $\mathbf{z} \cdot \nabla \mathbf{y}$ term has when it is written on the right-hand side of the underlying advection–diffusion equation. For the MHD momentum equation, for example, the Lorentz force term has $\mathbf{y} = \mathbf{z} = \mathbf{b}$ and the minus sign for the associated kinetic energy flux (with $\mathbf{x} = \mathbf{u}$) should be absent. See §§ 2.1 and 4.2. When it is appropriate to do so, the minus sign and its propagation into other equations in this appendix is easily removed.

In the special case that $\tau^{\ell}(y_i, z_j)$ is index-symmetric, only the index-symmetric part of $\partial_j \bar{x}^{\ell}_i$ contributes. This is the situation for the kinetic energy flux in HD (Germano 1992) and by analogy in MHD, see e.g. Zhou & Vahala (1991), Kessar *et al.* (2016), Aluie (2017), Offermans *et al.* (2018) and Alexakis & Chibbaro (2022). In general, however, the index-antisymmetric part of $\partial_j \bar{x}^{\ell}_i$ is also needed.

As shown by Johnson (2021), (A2) may also be expressed entirely in terms of (products of) the gradient tensors for $\mathbf{x}$, $\mathbf{y}$, $\mathbf{z}$ and integrals over them. Denoting the respective gradient tensors as $\partial_j x_i = X_{ij}$, $\partial_j y_i = Y_{ij}$ and $\partial_j z_i = Z_{ij}$, we have

$$\Pi^{\ell}_{xyz} = -\ell^2 \bar{X}^{\ell}_{ij} \bar{Y}^{\ell}_{ik} \bar{Z}^{\ell}_{jk} - \bar{X}^{\ell}_{ij} \int_0^{\ell^2} \mathrm{d}\theta \left(\overline{\overline{Y}^{\sqrt{\theta}}_{ik} \overline{Z}^{\sqrt{\theta}}_{jk}}^{\phi} - \overline{\overline{Y}^{\sqrt{\theta}}_{ik}}^{\phi} \overline{\overline{Z}^{\sqrt{\theta}}_{jk}}^{\phi} \right) \tag{A3}$$

$$= \Pi^{\ell}_{s,xyz} + \Pi^{\ell}_{m,xyz}, \tag{A4}$$

where $\phi = \sqrt{\ell^2 - \theta}$ and $\sqrt{\theta}$ correspond to all filter scales smaller than ℓ, and the subscripts s and m stand for single-scale and multi-scale. Equivalently, expressed in terms of the matrix trace operation, this is

$$\Pi^{\ell}_{xyz} = -\ell^2 \mathrm{Tr}\left\{ (\bar{\mathsf{X}}^{\ell})^t \bar{\mathsf{Y}}^{\ell} (\bar{\mathsf{Z}}^{\ell})^t \right\} - \int_0^{\ell^2} \mathrm{d}\theta \mathrm{Tr}\left\{ (\overline{\mathsf{X}}^{\ell})^t \left[\overline{\overline{\mathsf{Y}}^{\sqrt{\theta}} (\overline{\mathsf{Z}}^{\sqrt{\theta}})^t}^{\phi} - \overline{\overline{\mathsf{Y}}^{\sqrt{\theta}}}^{\phi} \overline{(\overline{\mathsf{Z}}^{\sqrt{\theta}})^t}^{\phi} \right] \right\}. \tag{A5}$$

Thus, both the single-scale and the multi-scale terms may be expressed as (integrals of) the trace of the appropriate filterings and transposes of the product of the three gradient tensors.

Splitting the gradient tensors into their index symmetric and antisymmetric parts, e.g. $\overline{\mathbf{X}}^{\ell} = \overline{\mathbf{S}}^{\ell}_X + \overline{\Omega}^{\ell}_X$, produces a decomposition of (A5) that facilitates physical interpretation of the subterms. For the single-scale terms, one has, modulo the $-\ell^2$ factor,

$$\mathrm{Tr}\left\{ \left(\bar{\mathbf{X}}^{\ell}\right)^t \bar{\mathbf{Y}}^{\ell} \left(\bar{\mathbf{Z}}^{\ell}\right)^t \right\}$$

$$= \mathrm{Tr}\left\{ \left(\bar{\mathbf{S}}^{\ell}_X - \bar{\boldsymbol{\Omega}}^{\ell}_X\right) \left(\bar{\mathbf{S}}^{\ell}_Y \bar{\mathbf{S}}^{\ell}_Z + \bar{\boldsymbol{\Omega}}^{\ell}_Y \bar{\mathbf{S}}^{\ell}_Z - \bar{\mathbf{S}}^{\ell}_Y \bar{\boldsymbol{\Omega}}^{\ell}_Z - \bar{\boldsymbol{\Omega}}^{\ell}_Y \bar{\boldsymbol{\Omega}}^{\ell}_Z \right) \right\} \tag{A6}$$

$$= \mathrm{Tr}\left\{ \bar{\mathbf{S}}^{\ell}_X \bar{\mathbf{S}}^{\ell}_Y \bar{\mathbf{S}}^{\ell}_Z + \left(\bar{\mathbf{S}}^{\ell}_X - \bar{\boldsymbol{\Omega}}^{\ell}_X\right) \left(\bar{\boldsymbol{\Omega}}^{\ell}_Y \bar{\mathbf{S}}^{\ell}_Z - \bar{\mathbf{S}}^{\ell}_Y \bar{\boldsymbol{\Omega}}^{\ell}_Z\right) + \bar{\boldsymbol{\Omega}}^{\ell}_X \bar{\boldsymbol{\Omega}}^{\ell}_Y \bar{\boldsymbol{\Omega}}^{\ell}_Z - \bar{\mathbf{S}}^{\ell}_X \bar{\boldsymbol{\Omega}}^{\ell}_Y \bar{\boldsymbol{\Omega}}^{\ell}_Z - \bar{\boldsymbol{\Omega}}^{\ell}_X \bar{\mathbf{S}}^{\ell}_Y \bar{\mathbf{S}}^{\ell}_Z \right\}, \tag{A7}$$

which in general does not simplify further.

https://doi.org/10.1017/S0022377824000898 Published online by Cambridge University Press

Simplifications do ensue, however, for special cases when one or more of $\mathbf{X}$, $\mathbf{Y}$, $\mathbf{Z}$ are equal. One makes use of matrix properties like $\boldsymbol{\Omega}_Y\mathbf{S}_Y + \mathbf{S}_Y^t\boldsymbol{\Omega}_Y^t$ is a symmetric matrix and the square of any (square) matrix is a symmetric matrix. For example, when $\mathbf{Y} = \mathbf{Z}$, as is relevant for the Inertial ($\Pi_s^{I,\ell}$) and Maxwell ($\Pi_s^{M,\ell}$) fluxes, we obtain

$$\mathrm{Tr}\left\{\left(\bar{\mathbf{X}}^\ell\right)^t\bar{\mathbf{Y}}^\ell\left(\bar{\mathbf{Y}}^\ell\right)^t\right\} = \mathrm{Tr}\left\{\bar{\mathbf{S}}_X^\ell\bar{\mathbf{S}}_Y^\ell\bar{\mathbf{S}}_Y^\ell - \bar{\mathbf{S}}_X^\ell\bar{\boldsymbol{\Omega}}_Y^\ell\bar{\boldsymbol{\Omega}}_Y^\ell + \bar{\mathbf{S}}_X^\ell\left[\bar{\boldsymbol{\Omega}}_Y^\ell\bar{\mathbf{S}}_Y^\ell + \left(\bar{\boldsymbol{\Omega}}_Y^\ell\bar{\mathbf{S}}_Y^\ell\right)^t\right]\right\}. \tag{A8}$$

Examples with $\mathbf{X} = \mathbf{Y}$ and $\mathbf{X} = \mathbf{Z}$ relate to the Advection and Dynamo magnetic energy SGS fluxes. See § 4.3.

Turning to the multi-scale contributions in (A3), these may of course be similarly decomposed. Since the filtering operation is linear, the integrand can be split into the sum of four terms that each have the same structure as the original integrand, e.g.

$$\tau^\phi\left(\bar{\mathbf{S}}_Y^{\sqrt{\theta}}, \bar{\boldsymbol{\Omega}}_Z^{\sqrt{\theta}}\right) = \overline{\bar{\mathbf{S}}_Y^{\sqrt{\theta}}\,\overline{\boldsymbol{\Omega}}_Z^{\sqrt{\theta}}}^\phi - \overline{\bar{\mathbf{S}}_Y^{\sqrt{\theta}}}^\phi\,\overline{\overline{\boldsymbol{\Omega}}_Z^{\sqrt{\theta}}}^\phi. \tag{A9}$$

After integration and contraction with $\left(\overline{\mathbf{X}}^\ell\right)^t = \overline{\mathbf{S}}_X^\ell - \overline{\boldsymbol{\Omega}}_X^\ell$, this gives eight, in general distinct, multi-scale contributions. Once again, special cases such as $\mathbf{Y} = \mathbf{Z}$ may mean some of these eight are zero, or equivalent or cancel. The needed particular instances are discussed in the subsections of § 4.

A.1. *Special cases*

Here, we list specific examples of (A2) that are relevant to the HD and/or MHD equations.

(i) $\boldsymbol{x}, \boldsymbol{y}, \boldsymbol{z} \to \boldsymbol{u}$. This yields the usual Navier–Stokes energy flux, $\Pi^\ell = -\overline{S}_{ij}^\ell\,\tau^\ell(u_i, u_j)$. Due to the index symmetry of the SGS stress tensor, only the symmetric part of the gradient tensor of . plays a direct role, as noted previously.

(ii) $\boldsymbol{y}, \boldsymbol{z} \to \boldsymbol{u}$; $\boldsymbol{x} \to \boldsymbol{\omega} = \nabla \times \boldsymbol{u}$, the vorticity. This corresponds to the Navier–Stokes helicity flux, $\Pi^{H,\ell} = -2\,\overline{S}_{\omega\,ij}^\ell\,\tau^\ell(u_i, u_j)$. As for the previous case, the symmetry of the SGS stress means that the flux can be written in terms of just the symmetric part of the gradient tensor of vorticity, namely $\overline{S}_{\omega\,ij}^\ell = (\partial_j\overline{\omega}_i^\ell + \partial_i\overline{\omega}_j^\ell)/2$.

(iii) $\boldsymbol{y} \to \boldsymbol{u}$, $\boldsymbol{z} \to \boldsymbol{b}$, $\boldsymbol{x} \to \boldsymbol{a}$ together with $\boldsymbol{y} \to \boldsymbol{b}$, $\boldsymbol{z} \to \boldsymbol{u} = \nabla \times \boldsymbol{a}$; $\boldsymbol{x} \to \boldsymbol{a}$, where $\boldsymbol{a}$ such that $\boldsymbol{b} = \nabla \times \boldsymbol{a}$ is the magnetic vector potential. Here, the flux is that for the MHD magnetic helicity, $\Pi^{B,\ell} = -2\,\partial_j\overline{a}_i^\ell\left(\tau^\ell(u_i, b_j) - \tau^\ell(b_i, u_j)\right)$.

(iv) $\boldsymbol{x}, \boldsymbol{y}, \boldsymbol{z} \in \{\boldsymbol{u}, \boldsymbol{b}\}$: MHD kinetic energy, magnetic energy and cross-helicity fluxes. Regarding the energy fluxes, their exact decompositions and quantifications are discussed in detail in the main body of this work. Decomposition of the MHD helicity fluxes will be examined in a future paper.

(v) As an additional level of analysis, we may also consider various projections of the fields onto subspaces of particular interest. For instance, after decomposing the velocity field – using a basis constructed from eigenfunctions of the curl operator – into positively and negatively helical fields $\boldsymbol{u}^\pm$, such that $\boldsymbol{u} = \boldsymbol{u}^+ + \boldsymbol{u}^-$ (Waleffe 1993; Lessinnes *et al.* 2011; Linkmann *et al.* 2015; Alexakis 2017; Alexakis & Biferale 2018; Yang *et al.* 2021), the following SGS stresses occur in the evolution

https://doi.org/10.1017/S0022377824000898 Published online by Cambridge University Press

equations for .:

$$\tau_{ij}^{\ell}(\boldsymbol{u}^{\pm},\boldsymbol{u}^{\pm}) = \overline{u_i^{\pm}u_j^{\pm}}^{\ell} - \overline{u_i^{\pm}}^{\ell}\overline{u_j^{\pm}}^{\ell}, \tag{A10}$$

$$\tau_{ij}^{\ell}(\boldsymbol{u}^{\pm},\boldsymbol{u}^{\mp}) = \overline{u_i^{\pm}u_j^{\mp}}^{\ell} - \overline{u_i^{\pm}}^{\ell}\overline{u_j^{\mp}}^{\ell}, \tag{A11}$$

$$\tau_{ij}^{\ell}(\boldsymbol{u}^{\mp},\boldsymbol{u}^{\pm}) = \overline{u_i^{\mp}u_j^{\pm}}^{\ell} - \overline{u_i^{\mp}}^{\ell}\overline{u_j^{\pm}}^{\ell}. \tag{A12}$$

Appendix B. Two extended Betchov relations for MHD

Here, we derive two MHD analogues of the exact kinematic relation between components of the velocity-gradient tensor introduced by Betchov (1956) and use them to obtain relations between several MHD energy subfluxes.

Recall that Betchov (1956) showed that $\langle A_{ij}A_{jk}A_{ki}\rangle$, where $A_{ij}=\partial_j u_i$, etc. As a first step, we wish to prove a similar relation between gradients of filtered fields, where the filtering scale on each field need not be the same. Specifically, we demonstrate that

$$\left\langle \bar{A}_{ij}^{\ell}\bar{B}_{jk}^{m}\bar{B}_{ki}^{m}\right\rangle = 0, \tag{B1}$$

where ℓ, m are two generic filtering scales, and $B_{ij}=\partial_j b_i$ is an (unfiltered) gradient tensor related to a solenoidal magnetic field. The above gradient tensors can be, in principle, calculated in different positions.[4] Using incompressibility and periodic boundary conditions one obtains

$$\begin{aligned}\left\langle \bar{A}_{ij}^{\ell}\bar{B}_{jk}^{m}\bar{B}_{ki}^{m}\right\rangle = \left\langle \partial_i\left(\bar{A}_{ij}^{\ell}\bar{B}_{jk}^{m}\bar{b}_{k}^{m}\right)\right\rangle - \left\langle \partial_k\left(\bar{A}_{ij}^{\ell}\bar{B}_{ji}^{m}\bar{b}_{k}^{m}\right)\right\rangle + \left\langle \partial_j\left(\bar{A}_{ik}^{\ell}\bar{B}_{ji}^{m}\bar{b}_{k}^{m}\right)\right\rangle \\ - \left\langle \bar{A}_{ik}^{\ell}\bar{B}_{ji}^{m}\bar{B}_{kj}^{m}\right\rangle.\end{aligned} \tag{B2}$$

This yields (B1) since the averages of the gradients vanish when the boundary conditions are periodic (or the system is homogeneous), and we are left with a quantity equal to its negative.

The next step is to decompose each gradient tensor of (B1) in terms of its symmetric and antisymmetric parts:

$$\left\langle \left(\bar{S}_{ij}^{\ell}+\bar{\Omega}_{ij}^{\ell}\right)\left(\bar{\Sigma}_{jk}^{m}+\bar{J}_{jk}^{m}\right)\left(\bar{\Sigma}_{ki}^{m}+\bar{J}_{ki}^{m}\right)\right\rangle = 0. \tag{B3}$$

Exploiting the symmetries of the tensors involved yields the identity

$$-\left\langle \bar{S}_{ij}^{\ell}\bar{\Sigma}_{jk}^{m}\bar{\Sigma}_{ki}^{m}\right\rangle = \left\langle \bar{S}_{ij}^{\ell}\bar{J}_{jk}^{m}\bar{J}_{ki}^{m}\right\rangle + 2\left\langle \bar{\Omega}_{ij}^{\ell}\bar{\Sigma}_{jk}^{m}\bar{J}_{ki}^{m}\right\rangle. \tag{B4}$$

This can be considered as a generalised Betchov identity for MHD. As a special case, we note that if the magnetic field becomes equal to the velocity field and we remove the filters, then (B4) collapses to the standard Betchov relation.

Equation (B4) is multi-scale but not in the form of energy fluxes. To obtain such a relation, we calculate its convolution with the Gaussian filter, with filter scale $\phi = \sqrt{\ell^2-m^2}$, and integrate over the filter scale m, following what was done in the right-hand side of (2.15). The result is

$$\left\langle \Pi_{m,S\Sigma\Sigma}^{M,\ell}\right\rangle = \left\langle \Pi_{m,SJJ}^{M,\ell}\right\rangle + 2\left\langle \Pi_{m,\Omega\Sigma J}^{M,\ell}\right\rangle, \tag{B5}$$

which corresponds to (4.6) in the main body of the paper. The single-scale version of this relation (m subscripts replaced with s) also holds, as can be seen by setting $\ell = m$ in (B4),

[4] For instance, $\langle \overline{A_{ij}}^{\ell}(\boldsymbol{x},t)\,\overline{B_{jk}}^{m}(\boldsymbol{x}+\boldsymbol{r}',t)\,\overline{B_{ki}}^{m}(\boldsymbol{x}+\boldsymbol{r}'',t)\rangle$, where $\boldsymbol{r}', \boldsymbol{r}''$ are displacement vectors.

https://doi.org/10.1017/S0022377824000898 Published online by Cambridge University Press

i.e.

$$\left\langle \Pi^{M,\ell}_{s,S\Sigma\Sigma} \right\rangle = \left\langle \Pi^{M,\ell}_{s,SJJ} \right\rangle - 2\left\langle \Pi^{A,\ell}_{s,J\Sigma\Omega} \right\rangle. \tag{B6}$$

Note that this mixes terms from the momentum equation with one from the induction equation, with the last term being equivalent to $\langle \Pi^{M,\ell}_{s,\Omega\Sigma J} \rangle$ by the cyclic property of the trace.

In § 4.2, we infer from the simulation p.d.f.s that $\Pi^{M,\ell}_{m,S\Sigma\Sigma} \approx \Pi^{M,\ell}_{m,SJJ}$, where both these terms appear as averaged quantities in (B5). We can recover the pointwise identity relative to the subfluxes appearing in (B5) taking into account the (not averaged) gradients from the right-hand side of (B2). As a consequence, $\Pi^{M,\ell}_{m,\Omega\Sigma J}$ should be cancelled by the contribution from the gradients.

In addition to (B1), we can prove another exact identity that reads

$$\left\langle \bar{B}^{\ell}_{ij} \left(\bar{B}^{m}_{jk} \bar{A}^{m}_{ki} + \bar{A}^{m}_{jk} \bar{B}^{m}_{ki} \right) \right\rangle = 0. \tag{B7}$$

This is obtained by employing incompressibility and periodic boundary conditions on

$$\begin{aligned} \left\langle \bar{B}^{\ell}_{ij} \bar{B}^{m}_{jk} \bar{A}^{m}_{ki} \right\rangle = & \left\langle \partial_k \left(\bar{b}^{\ell}_{i} \bar{B}^{m}_{kj} \bar{A}^{m}_{ji} \right) \right\rangle - \left\langle \partial_j \left(\bar{b}^{\ell}_{i} \bar{b}^{m}_{k} \bar{u}^{m}_{j,ik} \right) \right\rangle \\ & + \left\langle \partial_i \left(\bar{B}^{\ell}_{ij} \bar{b}^{m}_{k} \bar{A}^{m}_{jk} \right) \right\rangle - \left\langle \bar{B}^{\ell}_{ij} \bar{A}^{m}_{jk} \bar{B}^{m}_{ki} \right\rangle. \end{aligned} \tag{B8}$$

Clearly, the structure of this term may be of interest for Advection and Dynamo subfluxes. Decomposing each gradient tensor in terms of the symmetric and antisymmetric parts yields

$$\left\langle \bar{\Sigma}^{\ell}_{ij} \bar{\Sigma}^{m}_{jk} \bar{S}^{m}_{ki} \right\rangle + \left\langle \bar{\Sigma}^{\ell}_{ij} \bar{J}^{m}_{jk} \bar{\Omega}^{m}_{ki} \right\rangle + \left\langle \bar{J}^{\ell}_{ij} \bar{\Sigma}^{m}_{jk} \bar{\Omega}^{m}_{ki} \right\rangle + \left\langle \bar{J}^{\ell}_{ij} \bar{J}^{m}_{jk} \bar{S}^{m}_{ki} \right\rangle = 0, \tag{B9}$$

and, following manipulations similar to those yielding (B5), this can be mapped into a relation between subfluxes

$$\left\langle \Pi^{A,\ell}_{m,\Sigma\Sigma S} \right\rangle + \left\langle \Pi^{A,\ell}_{m,J\Sigma\Omega} \right\rangle = \left\langle \Pi^{A,\ell}_{m,\Sigma J\Omega} \right\rangle + \left\langle \Pi^{A,\ell}_{m,JJS} \right\rangle, \tag{B10}$$

whose single-scale counterpart coincides with (B6). These two relations may be used to write the decomposition of the total MHD energy flux more compactly and to assist with physical interpretations.

B.1. *Further observations*

From figure 6, it can be observed that the multi-scale terms $\langle \Pi^{M,\ell}_{m,S\Sigma\Sigma} \rangle$ and $\langle \Pi^{M,\ell}_{m,SJJ} \rangle$ are approximately equal, albeit being very small compared with terms of type $SJ\Sigma$. This is reminiscent of the similar relation for two multi-scale Inertial subfluxes discussed in § 4.1. However, in the present case, the structure of the fields is different since the subfluxes of $\Pi^{M,\ell}$ are formed from one velocity gradient tensor and two magnetic gradient tensors.

Since our numerical results indicate that $\langle \Pi^{M,\ell}_{m,S\Sigma\Sigma} \rangle \approx \langle \Pi^{M,\ell}_{m,SJJ} \rangle$, (4.6) implies that $\langle \Pi^{M,\ell}_{m,\Omega\Sigma J} \rangle \approx 0$, as is also seen for the $\Pi^{I,\ell}_{m,\Omega S\Omega}$ Inertial term (in both the HD and MHD cases) that has the same symmetric/antisymmetric tensorial structure. Equation (4.6) reveals that the difference between $\langle \Pi^{M,\ell}_{m,S\Sigma\Sigma} \rangle$ and $\langle \Pi^{M,\ell}_{m,SJJ} \rangle$ is governed by $\langle \Pi^{M,\ell}_{m,\Omega\Sigma J} \rangle$, a term that does not contribute to the energy balance, because in (2.9), only the symmetric part of the gradient tensor survives after the contraction with the symmetric SGS stress $\tau^{\ell}(b_i, b_j)$. Thus, we may posit a physical explanation for why $\langle \Pi^{M,\ell}_{m,\Omega\Sigma J} \rangle \approx 0$ by arguing that the values of $\langle \Pi^{M,\ell}_{m,S\Sigma\Sigma} \rangle$ and $\langle \Pi^{M,\ell}_{m,SJJ} \rangle$ are essentially determined by the energy balance of the system, and hence cannot be altered by a quantity that does not contribute to this.

https://doi.org/10.1017/S0022377824000898 Published online by Cambridge University Press

Furthermore, we observe in figure 7(*b*) that the p.d.f.s for $\Pi^{M,\ell}_{m,S\Sigma\Sigma}$ and $\Pi^{M,\ell}_{m,SJJ}$ are roughly coincident, especially along the tails. Recall that a similar feature was seen with the analogous Inertial multi-scale subfluxes. Further quantitative confirmation of this approximate congruence is given by the similarity of the relevant moments listed in table 2. These types of approximate identity hold when there is an interplay of either three velocity gradient tensors (Inertial term – HD and MHD) or one velocity and two magnetic gradient tensor (Maxwell term). However, they do not occur when we study the same structure of subfluxes associated with one vorticity and two velocity gradient tensors in the context of helicity flux (see Capocci *et al.* (2023)). This suggests that the approximate identity is unlikely to be of kinematic origin, although the exact version, (4.6), is a kinematic result.

Appendix C. Two-dimensional MHD

C.1. *Algebraic setting*

In the 2-D case, we can express the strain-rate and rotation-rate tensors associated with the incompressible field $\mathbf{X} = (X_1, X_2)$ in the following way:

$$\mathbf{S}_X = \begin{pmatrix} \partial_1 X_1 & \dfrac{\partial_2 X_1 + \partial_1 X_2}{2} \\ \dfrac{\partial_2 X_1 + \partial_1 X_2}{2} & -\partial_1 X_1, \end{pmatrix} \tag{C1}$$

$$\boldsymbol{\Omega}_X = \frac{1}{2}\begin{pmatrix} 0 & \partial_2 X_1 - \partial_1 X_2 \\ -\partial_2 X_1 + \partial_1 X_2 & 0 \end{pmatrix} := \omega^X \begin{pmatrix} 0 & -1 \\ 1 & 0 \end{pmatrix}, \tag{C2}$$

where we have already enforced the incompressibility on the trace of (C1) and defined $\omega^X = (\partial_1 X_2 - \partial_2 X_1)$ to make the notation more compact. Given an additional incompressible field $\mathbf{Y}$, it is straightforward to verify that $\mathbf{S}_Y$ and $\boldsymbol{\Omega}_X$ satisfy the commutator algebra:

$$[\mathbf{S}_Y, \boldsymbol{\Omega}_X] = 2\ (\mathbf{S}_Y \cdot \boldsymbol{\Omega}_X)\,, \tag{C3}$$

where, unlike the general 3-D scenario, the product $\mathbf{S}_Y \cdot \boldsymbol{\Omega}_X$ is a symmetric and traceless tensor. It is also useful to note that the product of two strain-rate tensors related to different gradient tensors can be decomposed as the sum of a symmetric tensor and an antisymmetric one:

$$\begin{aligned} \mathbf{S}_X \cdot \mathbf{S}_Y = &\left(\partial_1 X_1 \partial_1 Y_1 + \frac{1}{4}\left(\partial_1 X_2 + \partial_2 X_1\right)\ \left(\partial_1 Y_2 + \partial_2 Y_1\right)\right) \cdot \mathbb{I} \\ &+ \frac{1}{2}\left(-\partial_1 X_1\ \left(\partial_1 Y_2 + \partial_2 Y_1\right) + \partial_1 Y_1\ \left(\partial_1 X_2 + \partial_2 X_1\right)\right) \cdot \begin{pmatrix} 0 & -1 \\ 1 & 0 \end{pmatrix} \qquad \text{(C4)} \\ &:= \sigma\left(\mathbf{X}, \mathbf{Y}\right) \mathbb{I} + \alpha\left(\mathbf{X}, \mathbf{Y}\right) \hat{\Omega}, \qquad \text{(C5)} \end{aligned}$$

where $\mathbb{I}$ is the 2×2 identity matrix and $\hat{\Omega}$ is the antisymmetric and traceless matrix that defines the 2-D rotation-rate tensor of (C2). The (scalar) auxiliary functions σ and α embody the functional part multiplying $\mathbb{I}$ and $\hat{\Omega}$, respectively; moreover, they are respectively symmetric and antisymmetric under argument exchange symmetry, i.e.

$$\alpha(\mathbf{X}, \mathbf{Y}) = -\alpha(\mathbf{Y}, \mathbf{X}), \quad \sigma(\mathbf{X}, \mathbf{Y}) = \sigma(\mathbf{Y}, \mathbf{X}). \tag{C 6}$$

Thus, if we swap the fields $\mathbf{X}$, $\mathbf{Y}$ in (C5), we obtain

$$\mathbf{S}_Y \cdot \mathbf{S}_X = \sigma\left(\mathbf{X}, \mathbf{Y}\right) \mathbb{I} - \alpha\left(\mathbf{X}, \mathbf{Y}\right) \hat{\Omega}. \tag{C7}$$

https://doi.org/10.1017/S0022377824000898 Published online by Cambridge University Press

In terms of tensor traces, the decomposition of (C5) and (C3) lead to three relevant identities, *viz.*:

$$\mathrm{Tr}\,\{\mathbf{S}_X\mathbf{S}_Y\mathbf{S}_Z\} = 0, \tag{C8}$$

$$\mathrm{Tr}\,\{\mathbf{S}_X\mathbf{S}_X\boldsymbol{\Omega}_Y\} = 0, \tag{C9}$$

$$\mathrm{Tr}\,\{\mathbf{S}_X\boldsymbol{\Omega}_Y\boldsymbol{\Omega}_Z\} = 0, \tag{C10}$$

where (C10) vanishes because $\boldsymbol{\Omega}_Y\,\boldsymbol{\Omega}_Z \propto \mathbb{I}$ and $\mathbf{S}_X$ is traceless.

With these properties in mind, we are ready to specialise (2.8)–(2.9) to the 2-D MHD situation. This will involve appropriate simplifications of the single/multi-scale decompositions like (2.17).

C.2. *SGS energy subfluxes*

As a consequence of (C8)–(C10), in both single-scale and multi-scale cases, the terms involving the contraction of either three strain-rate tensors, three rotation rate tensors, or one strain-rate and two rotation rate tensors vanish. Hence, the 2-D Inertial SGS flux is solely due to $\Pi^{I,\ell}_{m,S\Omega S}$ (Johnson 2021):

$$\Pi^{I,\ell} = -2\int_0^{\ell^2} \mathrm{d}\theta\ \mathrm{Tr}\left\{\bar{\mathbf{S}}^{\ell}\left[\overline{\overline{\boldsymbol{\Omega}}^{\sqrt{\theta}}\,\overline{\mathbf{S}}^{\sqrt{\theta}}}^{\phi} - \overline{\overline{\boldsymbol{\Omega}}^{\sqrt{\theta}}}^{\phi}\,\overline{\overline{\mathbf{S}}^{\sqrt{\theta}}}^{\phi}\right]\right\}. \tag{C11}$$

As mentioned in § 4.1, this is the only Inertial term that 'survives' in 3-D MHD (i.e. is not approximately zero; see figure 3), especially if we add a background magnetic field in the equations of motion (not shown).

The 2-D Maxwell flux contains one single-scale and one multi-scale term,

$$\Pi^{M,\ell} = -2\,\ell^2\mathrm{Tr}\left\{\bar{\mathbf{S}}^{\ell}\,\overline{\boldsymbol{\Sigma}}^{\ell}\,\bar{\mathbf{J}}^{\ell}\right\} + 2\int_0^{\ell^2} \mathrm{d}\theta\ \mathrm{Tr}\left\{\bar{\mathbf{S}}^{\ell}\left[\overline{\overline{\mathbf{J}}^{\sqrt{\theta}}\,\overline{\boldsymbol{\Sigma}}^{\sqrt{\theta}}}^{\phi} - \overline{\overline{\mathbf{J}}^{\sqrt{\theta}}}^{\phi}\,\overline{\overline{\boldsymbol{\Sigma}}^{\sqrt{\theta}}}^{\phi}\right]\right\}, \tag{C12}$$

and the Dynamo and the Advection fluxes formally contain two further multi-scale terms:

$$\begin{aligned}\Pi^{A,\ell} = {} & -2\,\ell^2\mathrm{Tr}\left\{\bar{\boldsymbol{\Sigma}}^{\ell}\,\bar{\mathbf{J}}^{\ell}\,\bar{\mathbf{S}}^{\ell}\right\} - \int_0^{\ell^2} \mathrm{d}\theta\ \mathrm{Tr}\left\{-\bar{\mathbf{J}}^{\ell}\left[\overline{\overline{\boldsymbol{\Sigma}}^{\sqrt{\theta}}\,\overline{\mathbf{S}}^{\sqrt{\theta}}}^{\phi} - \overline{\overline{\boldsymbol{\Sigma}}^{\sqrt{\theta}}}^{\phi}\,\overline{\overline{\mathbf{S}}^{\sqrt{\theta}}}^{\phi}\right]\right. \\ & \left. + \bar{\boldsymbol{\Sigma}}^{\ell}\left[\overline{\overline{\mathbf{J}}^{\sqrt{\theta}}\,\overline{\mathbf{S}}^{\sqrt{\theta}}}^{\phi} - \overline{\overline{\mathbf{J}}^{\sqrt{\theta}}}^{\phi}\,\overline{\overline{\mathbf{S}}^{\sqrt{\theta}}}^{\phi}\right] - \bar{\boldsymbol{\Sigma}}^{\ell}\left[\overline{\overline{\boldsymbol{\Sigma}}^{\sqrt{\theta}}\,\overline{\boldsymbol{\Omega}}^{\sqrt{\theta}}}^{\phi} - \overline{\overline{\boldsymbol{\Sigma}}^{\sqrt{\theta}}}^{\phi}\,\overline{\overline{\boldsymbol{\Omega}}^{\sqrt{\theta}}}^{\phi}\right]\right\},\end{aligned} \tag{C13}$$

$$\begin{aligned}\Pi^{D,\ell} = {} & \int_0^{\ell^2} \mathrm{d}\theta\ \mathrm{Tr}\left\{-\bar{\mathbf{J}}^{\ell}\left[\overline{\overline{\mathbf{S}}^{\sqrt{\theta}}\,\overline{\boldsymbol{\Sigma}}^{\sqrt{\theta}}}^{\phi} - \overline{\overline{\mathbf{S}}^{\sqrt{\theta}}}^{\phi}\,\overline{\overline{\boldsymbol{\Sigma}}^{\sqrt{\theta}}}^{\phi}\right]\right. \\ & \left. + \bar{\boldsymbol{\Sigma}}^{\ell}\left[\overline{\overline{\boldsymbol{\Omega}}^{\sqrt{\theta}}\,\bar{\boldsymbol{\Sigma}}^{\sqrt{\theta}}}^{\phi} - \overline{\overline{\boldsymbol{\Omega}}^{\sqrt{\theta}}}^{\phi}\,\overline{\overline{\boldsymbol{\Sigma}}^{\sqrt{\theta}}}^{\phi}\right] - \bar{\boldsymbol{\Sigma}}^{\ell}\left[\overline{\overline{\mathbf{S}}^{\sqrt{\theta}}\overline{\mathbf{J}}^{\sqrt{\theta}}}^{\phi} - \overline{\overline{\mathbf{S}}^{\sqrt{\theta}}}^{\phi}\,\overline{\overline{\mathbf{J}}^{\sqrt{\theta}}}^{\phi}\right]\right\}.\end{aligned} \tag{C14}$$

https://doi.org/10.1017/S0022377824000898 Published online by Cambridge University Press

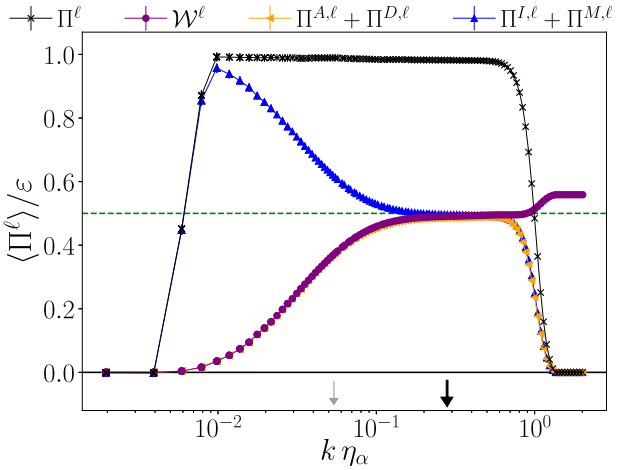

FIGURE 11. Scale-filtered fluxes for the kinetic and magnetic energy, normalised by the mean total energy dissipation rate $\varepsilon = \varepsilon_u + \varepsilon_b$, as a function of the adimensional parameter $k\eta_\alpha = \pi\eta_\alpha/\ell$. The p.d.f.s shown in figures 12–14 are calculated for the value of $k\eta_\alpha$ indicated by the thick (black) arrow, while the thin (grey) arrow denotes the value of $k\eta_\alpha$ used to calculate the p.d.f.s shown in § 4. Also shown is the kinetic–magnetic energy conversion term $\mathcal{W}^{\ell}$. The green dashed horizontal line corresponds to the y-axis value of 0.5. The error bars, although not fully visible, indicate one standard error.

After straightforward algebraic manipulations, we obtain the expression for Π^{ℓ} that corresponds to the total energy flux for 2-D MHD filtered at the scale ℓ:

$$\begin{aligned}\Pi^{\ell} &= \Pi^{I,\ell} + \Pi^{M,\ell} + \Pi^{D,\ell} + \Pi^{A,\ell} \\ &= -4\ell^2 \mathrm{Tr}\left\{\bar{\boldsymbol{\Sigma}}^{\ell}\,\bar{\mathbf{J}}^{\ell}\,\bar{\mathcal{S}}^{\ell}\right\} + 2\int_0^{\ell^2} \mathrm{d}\theta\ \mathrm{Tr}\left\{-\bar{\mathbf{S}}^{\ell}\left[\overline{\overline{\boldsymbol{\Omega}}^{\sqrt{\theta}}\,\overline{\mathbf{S}}^{\sqrt{\theta}}}^{\phi} - \overline{\overline{\boldsymbol{\Omega}}^{\sqrt{\theta}}}^{\phi}\,\overline{\overline{\mathbf{S}}^{\sqrt{\theta}}}^{\phi}\right]\right. \\ &\quad \left. + \bar{\mathbf{S}}^{\ell}\left[\overline{\overline{\mathbf{J}}^{\sqrt{\theta}}\,\overline{\boldsymbol{\Sigma}}^{\sqrt{\theta}}}^{\phi} - \overline{\overline{\mathbf{J}}^{\sqrt{\theta}}}^{\phi}\,\overline{\overline{\boldsymbol{\Sigma}}^{\sqrt{\theta}}}^{\phi}\right] + \bar{\mathbf{J}}^{\ell}\left[\overline{\overline{\boldsymbol{\Sigma}}^{\sqrt{\theta}}\,\overline{\mathbf{S}}^{\sqrt{\theta}}}^{\phi} - \overline{\overline{\boldsymbol{\Sigma}}^{\sqrt{\theta}}}^{\phi}\,\overline{\overline{\mathbf{S}}^{\sqrt{\theta}}}^{\phi}\right]\right\}. \end{aligned} \tag{C15}$$

Clearly, this has one single-scale and three distinct multi-scale contributions.

Appendix D. Equipartition subrange p.d.f.s

Here, we show some p.d.f.s for the MHD energy subfluxes for a filter scale that lies in the region where there is approximate equipartition between the magnetic and kinetic energy fluxes. The p.d.f.s presented in the main body of the paper are calculated for a larger scale.

Figure 11 displays the net kinetic energy flux, $\Pi^{I,\ell} + \Pi^{M,\ell}$, and the net magnetic energy flux, $\Pi^{A,\ell} + \Pi^{D,\ell}$, obtained using the Fourier filter and dataset A1. In essence, it is a rearrangement of figure 2. An equipartition region is evident for $0.2 \lesssim k\eta_\alpha \lesssim 0.6$, where the magnetic and kinetic energy subfluxes reach approximately 50% of the total energy flux, as indicated by the green dashed line. See Bian & Aluie (2019) for a discussion of this feature. Moreover, this equipartition region is also the region where the conversion term . of (2.7) saturates and becomes scale-independent.

Figure 12 displays energy (sub)fluxes for MHD dataset A1 for the filter scale $k\eta_\alpha = 0.27$. Comparing these figures with those presented in § 4, it is apparent that the p.d.f.s in

https://doi.org/10.1017/S0022377824000898 Published online by Cambridge University Press

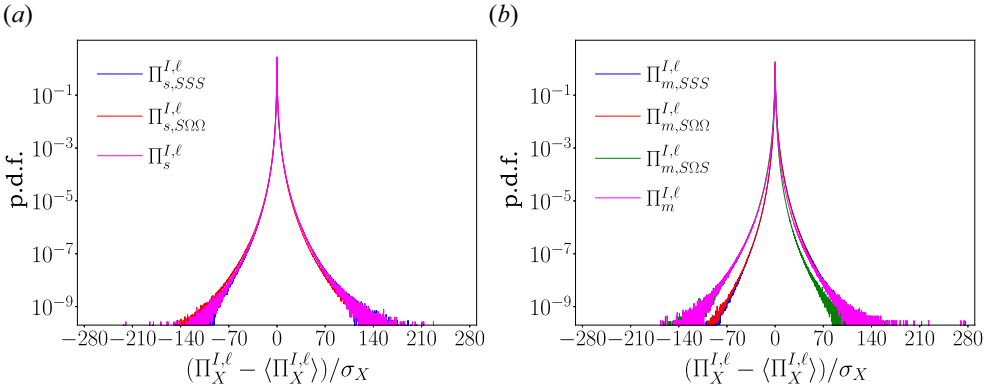

FIGURE 12. Standardised p.d.f.s of Inertial subfluxes $\Pi^{I,\ell}_X$ at $k\eta = 0.27$, where X represents the subflux identifier. (*a*) Single-scale fluxes; (*b*): multi-scale fluxes.

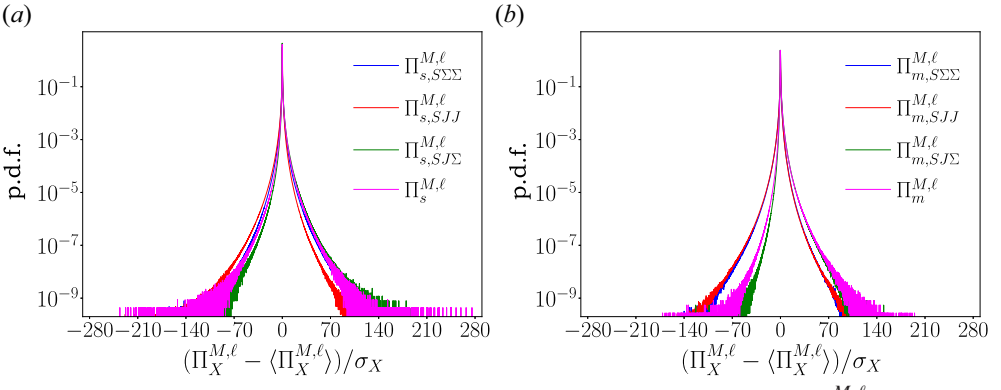

FIGURE 13. As for figure 12 but for the Maxwell energy fluxes, $\Pi^{M,\ell}_X$.

id	N	E_u	E_b	ν	ε_u	ε_b	L_u	τ	Re	$\eta/10^{-3}$	$k_{max}\eta^u$	$k_{max}\eta^b$	$\Delta t/\tau$	#
A4	2048	0.73	0.38	.	0.22	0.52	0.55	0.79	2144	1.8	1.68	1.35	1.1	18

TABLE 3. Simulation parameters and key observables for the standard diffusive MHD dataset A4; see definitions in table 1 setting $\alpha = 1$.

the equipartition region have fluctuations that are some three times larger. Recall that the p.d.f.s in figures 4, 7 and 10 were calculated for the larger scale $k\eta_\alpha = 5.4 \times 10^{-2}$. As we approach the dissipative range, the p.d.f.s develop even broader tails (not shown).

Appendix E. Comparison with standard diffusive MHD

The aim of this section is to repeat part of the analyses from §§ 3–4 on dataset A4 (see table 3) that employs the standard diffusive MHD equations. The results are discussed and compared with those from the hyper-dissipative run.

In figure 15, the kinetic and magnetic spectra of figure 1 and the standard diffusive MHD counterparts have been displayed together. Apart from the similarities concerning

https://doi.org/10.1017/S0022377824000898 Published online by Cambridge University Press

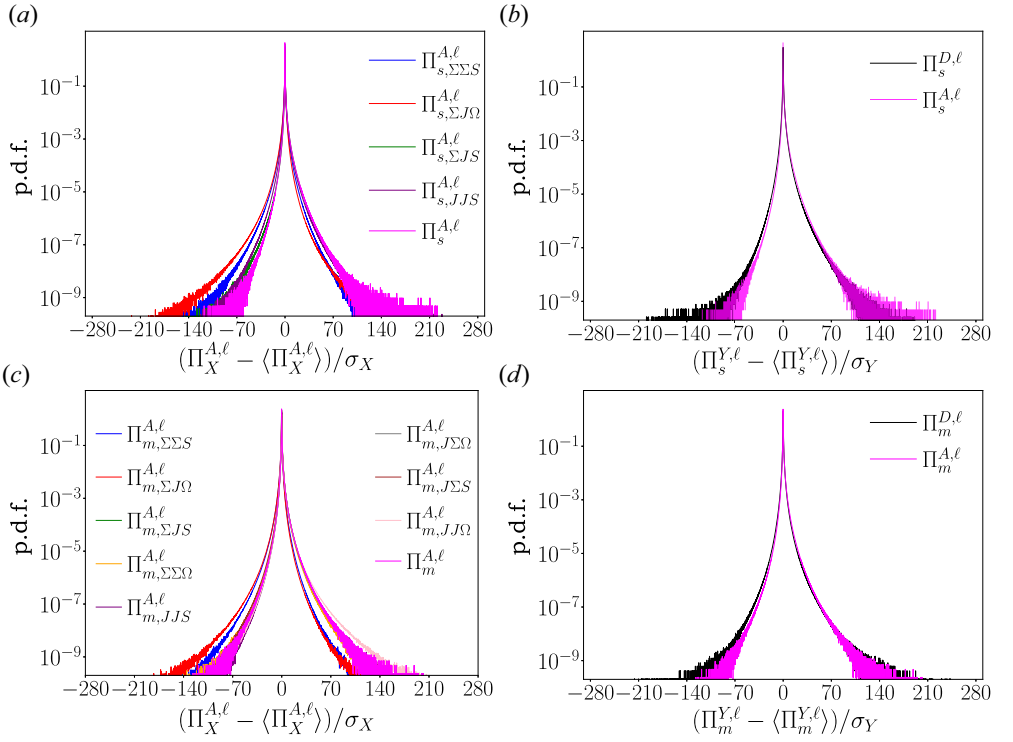

FIGURE 14. Standardised p.d.f.s. at $k\eta_\alpha = 0.27$. (*a*) Single-scale Advection subfluxes $\Pi_{s,X}^{A,\ell}$, where X represents the subflux identifier. (*b*) Single-scale net fluxes for the Dynamo and Advection terms, respectively $\Pi_s^{D,\ell}$ and $\Pi_s^{A,\ell}$, where $Y = D$ or A identifies the term. The subflux $\Pi_s^{A,\ell}$ is shown in both panels. (*c*,*d*) P.d.f.s of multi-scale Advection and Dynamo subfluxes, respectively.

the peaks and the large-scale behaviour (connected with the identical forcing scheme), we observe that spectra from standard viscosity dataset A4 present a shorter power-law scaling and a consequent smoother fall in the dissipative range. Nonetheless, corresponding spectra are qualitatively similar.

Figure 16 describes the net kinetic energy fluxes, $\Pi^{I,\ell} + \Pi^{M,\ell}$, and the net magnetic energy fluxes, $\Pi^{A,\ell} + \Pi^{D,\ell}$, obtained via employment of the Fourier filter on both the standard-diffusivity dataset A4 and the hyperviscous-diffusivity dataset A1. This plot can be considered as a rearrangement of figure 2, with the RSC term omitted. The most relevant difference between the two datasets is a striking reduction of the bandwidth of the inertial range related to dataset A4. From a subfluxes perspective, this feature is accompanied by the absence of an equipartition range: the magnetic and kinetic energy subfluxes do not each reach $\approx 50\%$ of the total energy flux, the level indicated by the green line.

With regards to the exact decomposition of the SGS stresses, the panels of figure 17 illustrate the standard-dissipation counterparts of figures 3(*b*), 6 and 8, which are being used as a comparison for the following analysis. Starting from panel (*a*), we notice a weaker depletion in the averaged Inertial transfer whose peak, at $k\eta \approx 0.01$, accounts for 20% of the total energy flux. We consider this feature to be a low-Re effect. To reinforce this view, we note that the maximum of $\langle \Pi^{I,\ell} \rangle$ increases as *Re* decreases (not shown) and

https://doi.org/10.1017/S0022377824000898 Published online by Cambridge University Press

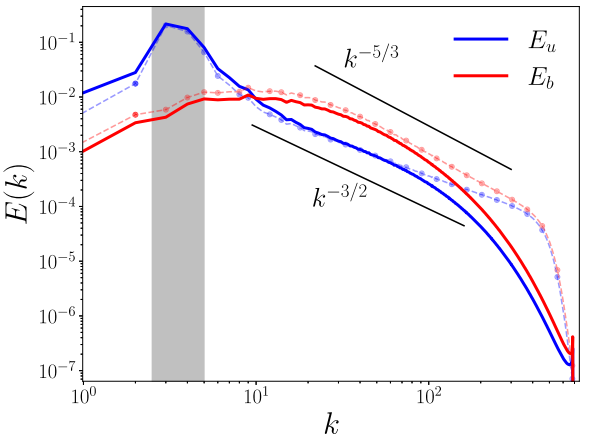

FIGURE 15. Time-averaged omnidirectional spectra for the velocity and magnetic field. The grey region indicates the wavenumber band where the velocity field is forced: $k \in [2.5, 5.0]$. The more transparent dotted curves have already been displayed in figure 1, while those characterised by a continuous line correspond to the standard viscosity dataset A4.

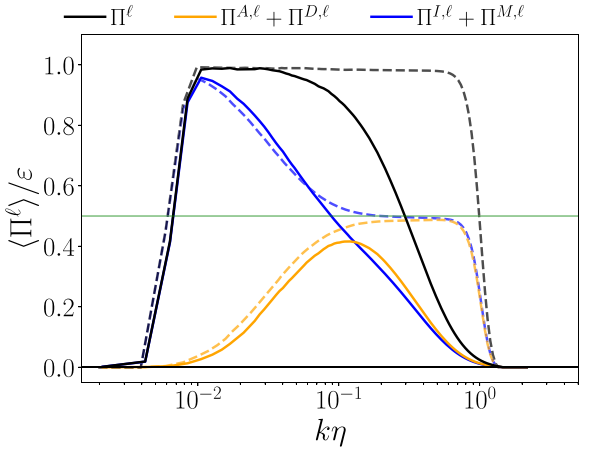

FIGURE 16. Scale-filtered fluxes for the mean kinetic and magnetic energy, normalised by the mean total energy dissipation rate $\varepsilon = \varepsilon_u + \varepsilon_b$, as a function of the adimensional parameter $k\eta = \pi\eta / \ell$. The dashed and more transparent curves refer to hyperviscous-diffusion dataset A1, while those identified by a continuous line are associated with standard-diffusive dataset A4.

that a similar profile in the mean Inertial transfer was already observed by Offermans *et al.* (2018). However, an increase in the Inertial transfer is compensated by an overall decrease of the Maxwell flux in panel (*b*), where the value of the latter is slightly reduced (relative to A1), diminishing even more as *Re* decreases (not shown). Moreover, $\Pi^{M,\ell}$ decays faster as $k\eta$ increases as a consequence of a shift towards the small-scales of the maximum of $\Pi^{M,\ell}_{s,SJ\Sigma}$ and to a less pronounced skewness of $\Pi^{M,\ell}_{m,SJ\Sigma}$. Thus, we conclude that these two effects are responsible for the lack of an equipartition range where the total kinetic subflux $\Pi^{I,\ell} + \Pi^{M,\ell}$ flattens reaching equipartition with the total magnetic flux $\Pi^{D,\ell} + \Pi^{A,\ell}$. Finally, both the total advection and dynamo subfluxes, respectively panels (*c*) and (*d*),

https://doi.org/10.1017/S0022377824000898 Published online by Cambridge University Press

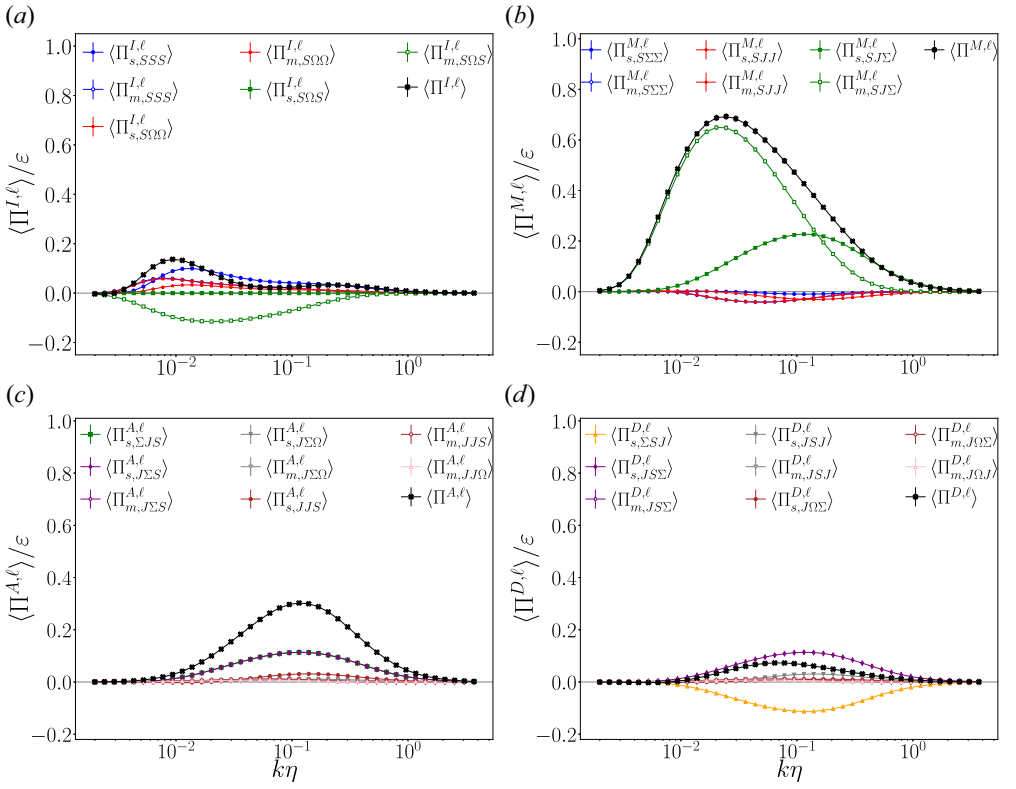

FIGURE 17. Decomposed fluxes for dataset A4 normalised by its mean total energy dissipation rate, ε. (*a*) Inertial term $\langle \Pi^{I,\ell} \rangle$, (*b*) Maxwell term $\langle \Pi^{M,\ell} \rangle$, (*c*) Advection term $\langle \Pi^{A,\ell} \rangle$ and (*d*) Dynamo term $\langle \Pi^{D,\ell} \rangle$. The error bars, although not visible, indicate one standard error.

present relatively decreased values at their peaks compared with the corresponding curves from hyperdissipative dataset A1; as expected, those maxima also keep decreasing with *Re* (not shown). In addition, $\langle \Pi^{A,\ell} \rangle$ shows, on logarithmic scale, a remarkable even-symmetry with respect to $k\eta \approx 0.12$ that can be extended to the coincident averages of $\Pi^{A,\ell}_{s,\Sigma JS}$ and $\Pi^{A,\ell}_{s,J\Sigma S}$. In conclusion, it is worth emphasising that the absence of a flattening region of the total magnetic subflux $\Pi^{A,\ell} + \Pi^{D,\ell}$ is ostensibly caused by a shift towards the large scales of the mean advection flux combined with a substantial reduction of the averaged total dynamo[5] subflux.

Appendix F. Subfluxes definitions

In this section, we provide the definitions of all the subfluxes appearing in the decomposition of the MHD energy fluxes. As highlighted in § 3, for the subfluxes $\Pi^{I,\ell}_{s,S\Omega S}$, $\Pi^{I,\ell}_{m,S\Omega S}$ and $\Pi^{M,\ell}_{s,SJ\Sigma}$, $\Pi^{M,\ell}_{m,SJ\Sigma}$, there is an extra factor of two that arises from the symmetry of the corresponding SGS stress tensors. Because in (2.6) and (2.7) the fluxes appear with the same leading signs, both the Maxwell and the Dynamo subfluxes in the definition below acquires an additional minus sign.

[5]Unlike the results for the hyper-dissipative dataset A1, those for the standard Laplacian dissipation run clearly indicate that, on average, the most negligible subflux is truly $\Pi^{D,\ell}$.

https://doi.org/10.1017/S0022377824000898 Published online by Cambridge University Press

F.1. *Inertial*

The following subfluxes are identical to the hydrodynamic counterpart from Johnson (2020, 2021):

$$\Pi^{I,\ell}_{s,SSS} = -\ell^2 \,\mathrm{Tr}\left\{\left(\bar{\mathbf{S}}^{\ell}\right)^{t}\,\bar{\mathbf{S}}^{\ell}\left(\bar{\mathbf{S}}^{\ell}\right)^{t}\right\}, \tag{F1}$$

$$\Pi^{I,\ell}_{m,SSS} = -\int_0^{\ell^2} \mathrm{d}\theta\,\mathrm{Tr}\left\{\left(\bar{\mathbf{S}}^{\ell}\right)^{t}\left(\overline{\overline{\mathbf{S}}^{\sqrt{\theta}}\left(\overline{\mathbf{S}}^{\sqrt{\theta}}\right)^{t}}^{\phi} - \overline{\overline{\mathbf{S}}^{\sqrt{\theta}}}^{\phi}\,\overline{\left(\overline{\mathbf{S}}^{\sqrt{\theta}}\right)^{t}}^{\phi}\right)\right\}, \tag{F2}$$

$$\Pi^{I,\ell}_{s,S\Omega\Omega} = -\ell^2 \,\mathrm{Tr}\left\{\left(\bar{\mathbf{S}}^{\ell}\right)^{t}\,\bar{\boldsymbol{\Omega}}^{\ell}\left(\bar{\boldsymbol{\Omega}}^{\ell}\right)^{t}\right\}, \tag{F3}$$

$$\Pi^{I,\ell}_{m,S\Omega\Omega} = -\int_0^{\ell^2} \mathrm{d}\theta\,\mathrm{Tr}\left\{\left(\bar{\mathbf{S}}^{\ell}\right)^{t}\left(\overline{\overline{\boldsymbol{\Omega}}^{\sqrt{\theta}}\left(\overline{\boldsymbol{\Omega}}^{\sqrt{\theta}}\right)^{t}}^{\phi} - \overline{\overline{\boldsymbol{\Omega}}^{\sqrt{\theta}}}^{\phi}\,\overline{\left(\overline{\boldsymbol{\Omega}}^{\sqrt{\theta}}\right)^{t}}^{\phi}\right)\right\}, \tag{F4}$$

$$\Pi^{I,\ell}_{s,S\Omega S} = -2\ell^2 \,\mathrm{Tr}\left\{\left(\bar{\mathbf{S}}^{\ell}\right)^{t}\,\bar{\boldsymbol{\Omega}}^{\ell}\left(\bar{\mathbf{S}}^{\ell}\right)^{t}\right\} \equiv 0, \tag{F5}$$

$$\Pi^{I,\ell}_{m,S\Omega S} = -2\int_0^{\ell^2} \mathrm{d}\theta\,\mathrm{Tr}\left\{\left(\bar{\mathbf{S}}^{\ell}\right)^{t}\left(\overline{\overline{\boldsymbol{\Omega}}^{\sqrt{\theta}}\left(\overline{\mathbf{S}}^{\sqrt{\theta}}\right)^{t}}^{\phi} - \overline{\overline{\boldsymbol{\Omega}}^{\sqrt{\theta}}}^{\phi}\,\overline{\left(\overline{\mathbf{S}}^{\sqrt{\theta}}\right)^{t}}^{\phi}\right)\right\}. \tag{F6}$$

F.2. *Maxwell*

$$\Pi^{M,\ell}_{s,S\Sigma\Sigma} = \ell^2 \,\mathrm{Tr}\left\{\left(\bar{\mathbf{S}}^{\ell}\right)^{t}\,\bar{\boldsymbol{\Sigma}}^{\ell}\left(\bar{\boldsymbol{\Sigma}}^{\ell}\right)^{t}\right\}, \tag{F7}$$

$$\Pi^{M,\ell}_{m,S\Sigma\Sigma} = \int_0^{\ell^2} \mathrm{d}\theta\,\mathrm{Tr}\left\{\left(\bar{\mathbf{S}}^{\ell}\right)^{t}\left(\overline{\overline{\boldsymbol{\Sigma}}^{\sqrt{\theta}}\left(\overline{\boldsymbol{\Sigma}}^{\sqrt{\theta}}\right)^{t}}^{\phi} - \overline{\overline{\boldsymbol{\Sigma}}^{\sqrt{\theta}}}^{\phi}\,\overline{\left(\overline{\boldsymbol{\Sigma}}^{\sqrt{\theta}}\right)^{t}}^{\phi}\right)\right\}, \tag{F8}$$

$$\Pi^{M,\ell}_{s,SJJ} = \ell^2 \,\mathrm{Tr}\left\{\left(\bar{\mathbf{S}}^{\ell}\right)^{t}\,\bar{\mathbf{J}}^{\ell}\left(\bar{\mathbf{J}}^{\ell}\right)^{t}\right\}, \tag{F9}$$

$$\Pi^{M,\ell}_{m,SJJ} = \int_0^{\ell^2} \mathrm{d}\theta\,\mathrm{Tr}\left\{\left(\bar{\mathbf{S}}^{\ell}\right)^{t}\left(\overline{\overline{\mathbf{J}}^{\sqrt{\theta}}\left(\overline{\mathbf{J}}^{\sqrt{\theta}}\right)^{t}}^{\phi} - \overline{\overline{\mathbf{J}}^{\sqrt{\theta}}}^{\phi}\,\overline{\left(\overline{\mathbf{J}}^{\sqrt{\theta}}\right)^{t}}^{\phi}\right)\right\}, \tag{F10}$$

$$\Pi^{M,\ell}_{s,SJ\Sigma} = 2\ell^2 \,\mathrm{Tr}\left\{\left(\bar{\mathbf{S}}^{\ell}\right)^{t}\,\bar{\mathbf{J}}^{\ell}\left(\bar{\boldsymbol{\Sigma}}^{\ell}\right)^{t}\right\}, \tag{F11}$$

$$\Pi^{M,\ell}_{m,SJ\Sigma} = 2\int_0^{\ell^2} \mathrm{d}\theta\,\mathrm{Tr}\left\{\left(\bar{\mathbf{S}}^{\ell}\right)^{t}\left(\overline{\overline{\mathbf{J}}^{\sqrt{\theta}}\left(\overline{\boldsymbol{\Sigma}}^{\sqrt{\theta}}\right)^{t}}^{\phi} - \overline{\overline{\mathbf{J}}^{\sqrt{\theta}}}^{\phi}\,\overline{\left(\overline{\boldsymbol{\Sigma}}^{\sqrt{\theta}}\right)^{t}}^{\phi}\right)\right\}. \tag{F12}$$

F.3. *Advection*

$$\Pi^{A,\ell}_{s,\Sigma\Sigma S} = -\ell^2 \,\mathrm{Tr}\left\{\left(\bar{\boldsymbol{\Sigma}}^{\ell}\right)^{t}\,\bar{\boldsymbol{\Sigma}}^{\ell}\left(\overline{\mathbf{S}}^{\ell}\right)^{t}\right\}, \tag{F13}$$

$$\Pi^{A,\ell}_{m,\Sigma\Sigma S} = -\int_0^{\ell^2} \mathrm{d}\theta\,\mathrm{Tr}\left\{\left(\bar{\boldsymbol{\Sigma}}^{\ell}\right)^{t}\left(\overline{\overline{\boldsymbol{\Sigma}}^{\sqrt{\theta}}\left(\overline{\mathbf{S}}^{\sqrt{\theta}}\right)^{t}}^{\phi} - \overline{\overline{\boldsymbol{\Sigma}}^{\sqrt{\theta}}}^{\phi}\,\overline{\left(\overline{\boldsymbol{\Sigma}}^{\sqrt{\theta}}\right)^{t}}^{\phi}\right)\right\}, \tag{F14}$$

https://doi.org/10.1017/S0022377824000898 Published online by Cambridge University Press

$$\Pi^{A,\ell}_{s,\Sigma JS} = -\ell^2 \,\mathrm{Tr}\left\{\left(\bar{\boldsymbol{\Sigma}}^{\ell}\right)^t \bar{\mathbf{J}}^{\ell}\left(\bar{\mathbf{S}}^{\ell}\right)^t\right\}, \tag{F15}$$

$$\Pi^{A,\ell}_{m,\Sigma JS} = -\int_0^{\ell^2} \mathrm{d}\theta \,\mathrm{Tr}\left\{\left(\bar{\boldsymbol{\Sigma}}^{\ell}\right)^t \left(\overline{\mathbf{J}^{\sqrt{\theta}}\left(\mathbf{S}^{\sqrt{\theta}}\right)^t}^{\phi} - \overline{\mathbf{J}^{\sqrt{\theta}}}^{\phi}\,\overline{\left(\mathbf{S}^{\sqrt{\theta}}\right)^t}^{\phi}\right)\right\}, \tag{F16}$$

$$\Pi^{A,\ell}_{s,\Sigma\Sigma\Omega} = -\ell^2 \,\mathrm{Tr}\left\{\left(\bar{\boldsymbol{\Sigma}}^{\ell}\right)^t \bar{\boldsymbol{\Sigma}}^{\ell}\left(\bar{\boldsymbol{\Omega}}^{\ell}\right)^t\right\} \equiv 0, \tag{F17}$$

$$\Pi^{A,\ell}_{m,\Sigma\Sigma\Omega} = -\int_0^{\ell^2} \mathrm{d}\theta \,\mathrm{Tr}\left\{\left(\bar{\boldsymbol{\Sigma}}^{\ell}\right)^t \left(\overline{\boldsymbol{\Sigma}^{\sqrt{\theta}}\left(\boldsymbol{\Omega}^{\sqrt{\theta}}\right)^t}^{\phi} - \overline{\boldsymbol{\Sigma}^{\sqrt{\theta}}}^{\phi}\,\overline{\left(\boldsymbol{\Omega}^{\sqrt{\theta}}\right)^t}^{\phi}\right)\right\}, \tag{F18}$$

$$\Pi^{A,\ell}_{s,\Sigma J\Omega} = -\ell^2 \,\mathrm{Tr}\left\{\left(\bar{\boldsymbol{\Sigma}}^{\ell}\right)^t \bar{\mathbf{J}}^{\ell}\left(\bar{\boldsymbol{\Omega}}^{\ell}\right)^t\right\}, \tag{F19}$$

$$\Pi^{A,\ell}_{m,\Sigma J\Omega} = -\int_0^{\ell^2} \mathrm{d}\theta \,\mathrm{Tr}\left\{\left(\bar{\boldsymbol{\Sigma}}^{\ell}\right)^t \left(\overline{\mathbf{J}^{\sqrt{\theta}}\left(\boldsymbol{\Omega}^{\sqrt{\theta}}\right)^t}^{\phi} - \overline{\mathbf{J}^{\sqrt{\theta}}}^{\phi}\,\overline{\left(\boldsymbol{\Omega}^{\sqrt{\theta}}\right)^t}^{\phi}\right)\right\}, \tag{F20}$$

$$\Pi^{A,\ell}_{s,J\Sigma S} = -\ell^2 \,\mathrm{Tr}\left\{\left(\bar{\mathbf{J}}^{\ell}\right)^t \bar{\boldsymbol{\Sigma}}^{\ell}\left(\bar{\mathbf{S}}^{\ell}\right)^t\right\}, \tag{F21}$$

$$\Pi^{A,\ell}_{m,J\Sigma S} = -\int_0^{\ell^2} \mathrm{d}\theta \,\mathrm{Tr}\left\{\left(\bar{\mathbf{J}}^{\ell}\right)^t \left(\overline{\boldsymbol{\Sigma}^{\sqrt{\theta}}\left(\mathbf{S}^{\sqrt{\theta}}\right)^t}^{\phi} - \overline{\boldsymbol{\Sigma}^{\sqrt{\theta}}}^{\phi}\,\overline{\left(\mathbf{S}^{\sqrt{\theta}}\right)^t}^{\phi}\right)\right\}, \tag{F22}$$

$$\Pi^{A,\ell}_{s,J\Sigma\Omega} = -\ell^2 \,\mathrm{Tr}\left\{\left(\bar{\mathbf{J}}^{\ell}\right)^t \bar{\boldsymbol{\Sigma}}^{\ell}\left(\bar{\boldsymbol{\Omega}}^{\ell}\right)^t\right\}, \tag{F23}$$

$$\Pi^{A,\ell}_{m,J\Sigma\Omega} = -\int_0^{\ell^2} \mathrm{d}\theta \,\mathrm{Tr}\left\{\left(\bar{\mathbf{J}}^{\ell}\right)^t \left(\overline{\boldsymbol{\Sigma}^{\sqrt{\theta}}\left(\boldsymbol{\Omega}^{\sqrt{\theta}}\right)^t}^{\phi} - \overline{\boldsymbol{\Sigma}^{\sqrt{\theta}}}^{\phi}\,\overline{\left(\boldsymbol{\Omega}^{\sqrt{\theta}}\right)^t}^{\phi}\right)\right\}, \tag{F24}$$

$$\Pi^{A,\ell}_{s,JJS} = -\ell^2 \,\mathrm{Tr}\left\{\left(\bar{\mathbf{J}}^{\ell}\right)^t \bar{\mathbf{J}}^{\ell}\left(\bar{\mathbf{S}}^{\ell}\right)^t\right\}, \tag{F25}$$

$$\Pi^{A,\ell}_{m,JJS} = -\int_0^{\ell^2} \mathrm{d}\theta \,\mathrm{Tr}\left\{\left(\bar{\mathbf{J}}^{\ell}\right)^t \left(\overline{\mathbf{J}^{\sqrt{\theta}}\left(\mathbf{S}^{\sqrt{\theta}}\right)^t}^{\phi} - \overline{\mathbf{J}^{\sqrt{\theta}}}^{\phi}\,\overline{\left(\mathbf{S}^{\sqrt{\theta}}\right)^t}^{\phi}\right)\right\}, \tag{F26}$$

$$\Pi^{A,\ell}_{s,JJ\Omega} = -\ell^2 \,\mathrm{Tr}\left\{\left(\bar{\mathbf{J}}^{\ell}\right)^t \bar{\mathbf{J}}^{\ell}\left(\bar{\boldsymbol{\Omega}}^{\ell}\right)^t\right\} \equiv 0, \tag{F27}$$

$$\Pi^{A,\ell}_{m,JJ\Omega} = -\int_0^{\ell^2} \mathrm{d}\theta \,\mathrm{Tr}\left\{\left(\bar{\mathbf{J}}^{\ell}\right)^t \left(\overline{\mathbf{J}^{\sqrt{\theta}}\left(\boldsymbol{\Omega}^{\sqrt{\theta}}\right)^t}^{\phi} - \overline{\mathbf{J}^{\sqrt{\theta}}}^{\phi}\,\overline{\left(\boldsymbol{\Omega}^{\sqrt{\theta}}\right)^t}^{\phi}\right)\right\}. \tag{F28}$$

F.4. *Dynamo*

$$\Pi^{D,\ell}_{s,\Sigma S\Sigma} = \ell^2 \,\mathrm{Tr}\left\{\left(\bar{\boldsymbol{\Sigma}}^{\ell}\right)^t \bar{\mathbf{S}}^{\ell}\left(\bar{\boldsymbol{\Sigma}}^{\ell}\right)^t\right\}, \tag{F29}$$

$$\Pi^{D,\ell}_{m,\Sigma S\Sigma} = \int_0^{\ell^2} \mathrm{d}\theta \,\mathrm{Tr}\left\{\left(\bar{\boldsymbol{\Sigma}}^{\ell}\right)^t \left(\overline{\mathbf{S}^{\sqrt{\theta}}\left(\boldsymbol{\Sigma}^{\sqrt{\theta}}\right)^t}^{\phi} - \overline{\mathbf{S}^{\sqrt{\theta}}}^{\phi}\,\overline{\left(\boldsymbol{\Sigma}^{\sqrt{\theta}}\right)^t}^{\phi}\right)\right\}, \tag{F30}$$

$$\Pi^{D,\ell}_{s,\Sigma\Omega\Sigma} = \ell^2 \,\mathrm{Tr}\left\{\left(\bar{\boldsymbol{\Sigma}}^{\ell}\right)^t \bar{\boldsymbol{\Omega}}^{\ell}\left(\bar{\boldsymbol{\Sigma}}^{\ell}\right)^t\right\} \equiv 0, \tag{F31}$$

https://doi.org/10.1017/S0022377824000898 Published online by Cambridge University Press

$$\Pi^{D,\ell}_{m,\Sigma\Omega\Sigma} = \int_0^{\ell^2} \mathrm{d}\theta\, \mathrm{Tr}\left\{ \left(\bar{\boldsymbol{\Sigma}}^{\ell}\right)^t \left(\overline{\overline{\boldsymbol{\Omega}}^{\sqrt{\theta}} \left(\overline{\boldsymbol{\Sigma}}^{\sqrt{\theta}}\right)^{t^{\phi}}} - \overline{\overline{\boldsymbol{\Omega}}^{\sqrt{\theta}}}^{\phi} \overline{\left(\overline{\boldsymbol{\Sigma}}^{\sqrt{\theta}}\right)^{t^{\phi}}} \right) \right\}, \tag{F32}$$

$$\Pi^{D,\ell}_{s,\Sigma SJ} = \ell^2\, \mathrm{Tr}\left\{ \left(\bar{\boldsymbol{\Sigma}}^{\ell}\right)^t \bar{\mathbf{S}}^{\ell} \left(\bar{\mathbf{J}}^{\ell}\right)^t \right\}, \tag{F33}$$

$$\Pi^{D,\ell}_{m,\Sigma SJ} = \int_0^{\ell^2} \mathrm{d}\theta\, \mathrm{Tr}\left\{ \left(\bar{\boldsymbol{\Sigma}}^{\ell}\right)^t \left(\overline{\overline{\mathbf{S}}^{\sqrt{\theta}} \left(\overline{\mathbf{J}}^{\sqrt{\theta}}\right)^{t^{\phi}}} - \overline{\overline{\mathbf{S}}^{\sqrt{\theta}}}^{\phi} \overline{\left(\overline{\mathbf{J}}^{\sqrt{\theta}}\right)^{t^{\phi}}} \right) \right\}, \tag{F34}$$

$$\Pi^{D,\ell}_{s,\Sigma\Omega J} = \ell^2\, \mathrm{Tr}\left\{ \left(\bar{\boldsymbol{\Sigma}}^{\ell}\right)^t \bar{\boldsymbol{\Omega}}^{\ell} \left(\bar{\mathbf{J}}^{\ell}\right)^t \right\}, \tag{F35}$$

$$\Pi^{D,\ell}_{m,\Sigma\Omega J} = \int_0^{\ell^2} \mathrm{d}\theta\, \mathrm{Tr}\left\{ \left(\bar{\boldsymbol{\Sigma}}^{\ell}\right)^t \left(\overline{\overline{\boldsymbol{\Omega}}^{\sqrt{\theta}} \left(\overline{\mathbf{J}}^{\sqrt{\theta}}\right)^{t^{\phi}}} - \overline{\overline{\boldsymbol{\Omega}}^{\sqrt{\theta}}}^{\phi} \overline{\left(\overline{\mathbf{J}}^{\sqrt{\theta}}\right)^{t^{\phi}}} \right) \right\}, \tag{F36}$$

$$\Pi^{D,\ell}_{s,JS\Sigma} = \ell^2\, \mathrm{Tr}\left\{ \left(\bar{\boldsymbol{J}}^{\ell}\right)^t \bar{\mathbf{S}}^{\ell} \left(\bar{\boldsymbol{\Sigma}}^{\ell}\right)^t \right\}, \tag{F37}$$

$$\Pi^{D,\ell}_{m,JS\Sigma} = \int_0^{\ell^2} \mathrm{d}\theta\, \mathrm{Tr}\left\{ \left(\bar{\mathbf{J}}^{\ell}\right)^t \left(\overline{\overline{\mathbf{S}}^{\sqrt{\theta}} \left(\overline{\boldsymbol{\Sigma}}^{\sqrt{\theta}}\right)^{t^{\phi}}} - \overline{\overline{\mathbf{S}}^{\sqrt{\theta}}}^{\phi} \overline{\left(\overline{\boldsymbol{\Sigma}}^{\sqrt{\theta}}\right)^{t^{\phi}}} \right) \right\}, \tag{F38}$$

$$\Pi^{D,\ell}_{s,J\Omega\Sigma} = \ell^2\, \mathrm{Tr}\left\{ \left(\bar{\mathbf{J}}^{\ell}\right)^t \bar{\boldsymbol{\Omega}}^{\ell} \left(\bar{\boldsymbol{\Sigma}}^{\ell}\right)^t \right\}, \tag{F39}$$

$$\Pi^{D,\ell}_{m,J\Omega\Sigma} = \int_0^{\ell^2} \mathrm{d}\theta\, \mathrm{Tr}\left\{ \left(\bar{\mathbf{J}}^{\ell}\right)^t \left(\overline{\overline{\boldsymbol{\Omega}}^{\sqrt{\theta}} \left(\overline{\boldsymbol{\Sigma}}^{\sqrt{\theta}}\right)^{t^{\phi}}} - \overline{\overline{\boldsymbol{\Omega}}^{\sqrt{\theta}}}^{\phi} \overline{\left(\overline{\boldsymbol{\Sigma}}^{\sqrt{\theta}}\right)^{t^{\phi}}} \right) \right\}, \tag{F40}$$

$$\Pi^{D,\ell}_{s,JSJ} = \ell^2\, \mathrm{Tr}\left\{ \left(\bar{\mathbf{J}}^{\ell}\right)^t \bar{\mathbf{S}}^{\ell} \left(\bar{\mathbf{J}}^{\ell}\right)^t \right\}, \tag{F41}$$

$$\Pi^{D,\ell}_{m,JSJ} = \int_0^{\ell^2} \mathrm{d}\theta\, \mathrm{Tr}\left\{ \left(\bar{\mathbf{J}}^{\ell}\right)^t \left(\overline{\overline{\mathbf{S}}^{\sqrt{\theta}} \left(\overline{\mathbf{J}}^{\sqrt{\theta}}\right)^{t^{\phi}}} - \overline{\overline{\mathbf{S}}^{\sqrt{\theta}}}^{\phi} \overline{\left(\overline{\mathbf{J}}^{\sqrt{\theta}}\right)^{t^{\phi}}} \right) \right\}, \tag{F42}$$

$$\Pi^{D,\ell}_{s,J\Omega J} = \ell^2\, \mathrm{Tr}\left\{ \left(\bar{\mathbf{J}}^{\ell}\right)^t \bar{\boldsymbol{\Omega}}^{\ell} \left(\bar{\mathbf{J}}^{\ell}\right)^t \right\} \equiv 0, \tag{F43}$$

$$\Pi^{D,\ell}_{m,J\Omega J} = \int_0^{\ell^2} \mathrm{d}\theta\, \mathrm{Tr}\left\{ \left(\bar{\mathbf{J}}^{\ell}\right)^t \left(\overline{\overline{\boldsymbol{\Omega}}^{\sqrt{\theta}} \left(\overline{\mathbf{J}}^{\sqrt{\theta}}\right)^{t^{\phi}}} - \overline{\overline{\boldsymbol{\Omega}}^{\sqrt{\theta}}}^{\phi} \overline{\left(\overline{\mathbf{J}}^{\sqrt{\theta}}\right)^{t^{\phi}}} \right) \right\}. \tag{F44}$$

REFERENCES

ADKINS, T., SCHEKOCHIHIN, A.A., IVANOV, P.G. & ROACH, C.M. 2022 Electromagnetic instabilities and plasma turbulence driven by electron-temperature gradient. *J. Plasma Phys.* **88**, 905880410.

ALEXAKIS, A. 2013 Large-scale magnetic fields in magnetohydrodynamic turbulence. *Phys. Rev. Lett.* **110**, 084502.

ALEXAKIS, A. 2017 Helically decomposed turbulence. *J. Fluid Mech.* **812**, 752–770.

ALEXAKIS, A. & BIFERALE, L. 2018 Cascades and transitions in turbulent flows. *Phys. Rep.* **767–769**, 1–101.

ALEXAKIS, A. & CHIBBARO, S. 2022 Local fluxes in magnetohydrodynamic turbulence. *J. Plasma Phys.* **88** (5), 905880515.

ALEXAKIS, A., MININNI, P.D. & POUQUET, A. 2005 Shell-to-shell energy transfer in magnetohydrodynamics. I. Steady state turbulence. *Phys. Rev.* E **72**.

https://doi.org/10.1017/S0022377824000898 Published online by Cambridge University Press

ALUIE, H. 2017 Coarse-grained incompressible magnetohydrodynamics: analyzing the turbulent cascades. *New J. Phys*. **19**, 025008.

ALUIE, H. & EYINK, G.L. 2009 Localness of energy cascade in hydrodynamic turbulence. II. Sharp spectral filter. *Phys. Fluids* **21**, 115108.

ALUIE, H. & EYINK, G.L. 2010 Scale locality of magnetohydrodynamic turbulence. *Phys. Rev. Lett*. **104**, 081101.

BATCHELOR, G.K. 1970 *The Theory of Homogeneous Turbulence*. Cambridge University Press.

BERESNYAK, A. 2019 MHD turbulence. *Liv. Rev. Comput. Astrophys*. **5** (1), 2.

BETCHOV, R. 1956 An inequality concerning the production of vorticity in isotropic turbulence. *J. Fluid Mech*. **1**, 497.

BIAN, X. & ALUIE, H. 2019 Decoupled cascades of kinetic and magnetic energy in magnetohydrodynamic turbulence. *Phys. Rev. Lett*. **122**, 135101.

BISKAMP, D. 2003 *Magnetohydrodynamic Turbulence*. Cambridge University Press.

BORUE, V. & ORSZAG, S.A. 1995 Self-similiar decay of three-dimensional homogeneous turbulence with hyperviscosity. *Phys. Rev.* E **51**, R856.

BORUE, V. & ORSZAG, S.A. 1998 Local energy flux and subgrid-scale statistics in three-dimensional turbulence. *J. Fluid Mech*. **366**, 1–31.

BRANDENBURG, A. & REMPEL, M. 2019 Reversed dynamo at small scales and large magnetic Prandtl number. *Astrophys. J*. **879**, 57.

BRANDENBURG, A., SOKOLOFF, D. & SUBRAMANIAN, K. 2012 Current status of turbulent dynamo theory. *Space Sci. Rev*. **169**, 123–157.

BRUNO, R. & CARBONE, V. 2013 The solar wind as a turbulence laboratory. *Living Rev. Sol. Phys*. **10**, 2.

BUZZICOTTI, M., ALUIE, H., BIFERALE, L. & LINKMANN, M. 2018 Energy transfer in turbulence under rotation. *Phys. Rev. Fluids* **3**, 034802.

CANUTO, C., HUSSAINI, M.Y., QUARTERONI, A. & ZANG, T.A. 1988 *Spectral Methods in Fluid Mechanics*. Springer.

CAPOCCI, D., JOHNSON, P.L., OUGHTON, S., BIFERALE, L. & LINKMANN, M. 2023 New exact Betchov-like relation for the helicity flux in homogeneous turbulence. *J. Fluid Mech*. **963**, R1.

CHEN, S., ECKE, R.E., EYINK, G.L., RIVERA, M., WAN, M. & XIAO, Z. 2006 Physical mechanism of the two-dimensional inverse energy cascade. *Phys. Rev. Lett*. **96**, 084502.

CHERNYSHOV, A.A., KARELSKY, K.V. & PETROSYAN, A.S. 2010 Forced turbulence in large-eddy simulation of compressible magnetohydrodynamic turbulence. *Phys. Plasmas* **17** (10), 102307.

CLARK, R.A., FERZIGER, J.H. & REYNOLDS, W.C. 1979 Evaluation of subgrid-scale models using an accurately simulated turbulent flow. *J. Fluid Mech*. **91** (1), 1–16.

DAR, G., VERMA, M.K. & ESWARAN, V. 2001 Energy transfer in two-dimensional magnetohydrodynamic turbulence: formalism and numerical results. *Physica* D **157**, 207–225.

DAVIDSON, P.A. 1999 Magnetohydrodynamics in materials processing. *Annu. Rev. Fluid Mech*. **31**, 273–300.

DAVIDSON, P.A. 2016 *Introduction to Magnetohydrodynamics*. Cambridge University Press.

DONZIS, D.A., YEUNG, P.K. & SREENIVASAN, K.R. 2008 Dissipation and enstrophy in isotropic turbulence: resolution effects and scaling in direct numerical simulations. *Phys. Fluids* **20**, 045108.

EYINK, G.L. 2006 Multi-scale gradient expansion of the turbulent stress tensor. *J. Fluid Mech*. **549**, 159–190.

FREIDBERG, J.P. 2007 *Plasma Physics and Fusion Energy*. Cambridge University Press.

GERMANO, M. 1992 Turbulence – the filtering approach. *J. Fluid Mech*. **238**, 325–336.

GOLDREICH, P. & SRIDHAR, S. 1995 Toward a theory of interstellar turbulence. II. Strong Alfvénic turbulence. *Astrophys. J*. **438**, 763–775.

GOLDREICH, P. & SRIDHAR, S. 1997 Magnetohydrodynamic turbulence revisited. *Astrophys. J*. **485**, 680–688.

GRETE, P., VLAYKOV, D.G., SCHMIDT, W. & SCHLEICHER, D.R.G. 2016 A nonlinear structural subgrid-scale closure for compressible MHD. II. *A priori* comparison on turbulence simulation data. *Phys. Plasmas* **23**.

HAMBA, F. & TSUCHIYA, M. 2010 Cross-helicity dynamo effect in magnetohydrodynamic turbulent channel flow. *Phys. Plasmas* **17** (1), 012301.

HAUGEN, N.E.L. & BRANDENBURG, A. 2006 Hydrodynamic and hydromagnetic energy spectra from large eddy simulations. *Phys. Fluids* **18**.

IVANOV, P.G., SCHEKOCHIHIN, A.A. & DORLAND, W. 2022 Dimits transition in three-dimensional ion-temperature-gradient turbulence. *J. Plasma Phys*. **88** (5), 905880506.

IVANOV, P.G., SCHEKOCHIHIN, A.A., DORLAND, W., FIELD, A.R. & PARRA, F.I. 2020 Zonally dominated dynamics and dimits threshold in curvature-driven ITG turbulence. *J. Plasma Phys*. **86** (5), 855860502.

JADHAV, K. & CHANDY, A.J. 2021 Large eddy simulations of high-magnetic Reynolds number magnetohydrodynamic turbulence for non-helical and helical initial conditions: a study of two sub-grid scale models. *Phys. Fluids* **33** (8), 085131.

JADHAV, K. & CHANDY, A.J. 2023 Large eddy simulations of inhomogeneous high-magnetic Reynolds number magnetohydrodynamic flows. *Phys. Fluids* **35** (7), 075109.

JOHNSON, P.L. 2020 Energy transfer from large to small scales in turbulence by multiscale nonlinear strain and vorticity interactions. *Phys. Rev. Lett*. **124**, 104501.

JOHNSON, P.L. 2021 On the role of vorticity stretching and strain self-amplification in the turbulence energy cascade. *J. Fluid Mech*. **922**, A3.

JOHNSON, P.L. 2022 A physics-inspired alternative to spatial filtering for large-eddy simulations of turbulent flows. *J. Fluid Mech*. **934**, A30.

JONES, C.A. 2011 Planetary magnetic fields and fluid dynamos. *Annu. Rev. Fluid Mech*. **43**, 583–614.

KESSAR, M., BALARAC, G. & PLUNIAN, F. 2016 The effect of subgrid-scale models on grid-scale/subgrid-scale energy transfers in large-eddy simulation of incompressible magnetohydrodynamic turbulence. *Phys. Plasmas* **23** (10).

KRAICHNAN, R.H. 1976 Eddy viscosity in two and three dimensions. *J. Atmos. Sci*. **33**, 1521–1536.

LEONARD, A. 1975 Energy cascade in large-eddy simulations of turbulent fluid flows. In *Adv. Geophys.*, vol. 18, pp. 237–248. Elsevier.

LESSINNES, T., PLUNIAN, F., STEPANOV, R. & CARATI, D. 2011 Dissipation scales of kinetic helicities in turbulence. *Phys. Fluids* **23**.

LINKMANN, M., BUZZICOTTI, M. & BIFERALE, L. 2018 Multi-scale properties of large eddy simulations: correlations between resolved-scale velocity-field increments and subgrid-scale quantities. *J. Turbul*. **19**, 493–527.

LINKMANN, M.F., BERERA, A., MCCOMB, W.D. & MCKAY, M.E. 2015 Nonuniversality and finite dissipation in decaying magnetohydrodynamic turbulence. *Phys. Rev. Lett*. **114**, 235001.

LINKMANN, M., SAHOO, G., MCKAY, M., BERERA, A. & BIFERALE, L. 2017 Effects of magnetic and kinetic helicities on the growth of magnetic fields in laminar and turbulent flows by helical fourier decomposition. *Astrophys. J*. **836** (1), 26.

MATTHAEUS, W.H., WAN, M., SERVIDIO, S., GRECO, A., OSMAN, K.T., OUGHTON, S. & DMITRUK, P. 2015 Intermittency, nonlinear dynamics, and dissipation in the solar wind and astrophysical plasmas. *Phil. Trans. R. Soc.* A **373**, 20140154.

MENEVEAU, C. & KATZ, J. 2000 Scale-invariance and turbulence models for large-eddy simulation. *Annu. Rev. Fluid Mech*. **32**, 1–32.

MEYRAND, R., KIYANI, K.H. & GALTIER, S. 2015 Weak magnetohydrodynamic turbulence and intermittency. *J. Fluid Mech*. **770**, R1.

MIESCH, M., MATTHAEUS, W., BRANDENBURG, A., PETROSYAN, A., POUQUET, A., CAMBON, C., JENKO, F., UZDENSKY, D., STONE, J., TOBIAS, S., *et al.* 2015 Large-eddy simulations of magnetohydrodynamic turbulence in heliophysics and astrophysics. *Space Sci. Rev*. **194**, 97–137.

MININNI, P.D., MONTGOMERY, D.C. & POUQUET, A. 2005 Numerical solutions of the three-dimensional magnetohydrodynamic alpha model. *Phys. Rev.* E **71**, 046304.

MININNI, P.D. & POUQUET, A. 2009 Finite dissipation and intermittency in magnetohydrodynamics. *Phys. Rev.* E **80**, 025401.

MIURA, H. & ARAKI, K. 2012 Coarse-graining study of homogeneous and isotropic hall magnetohydrodynamics turbulence. *Plasma Phys. Control. Fusion* **55**, 014012.

MIURA, H., ARAKI, K. & HAMBA, F. 2016 Hall effects and sug-gird-scale modelling in magnetohydrodynamic turbulence simulations. *J. Comput. Phys*. **316**, 385–395.

MIURA, H., HAMBA, F. & ITO, A. 2017 Two-fluid sub-grid-scale viscosity in nonlinear simulation of ballooning modes in a heliotron device. *Nucl. Fusion* **57**, 076034.

MÜLLER, W.-C. & CARATI, D. 2002 Dynamic gradient-diffusion subgrid models for incompressible magnetohydrodynamic turbulence. *Phys. Plasmas* **9** (3), 824–834.

MÜLLER, W.-C. & GRAPPIN, R. 2004 The residual energy in freely decaying magnetohydrodynamic turbulence. *Plasma Phys. Control. Fusion* **46** (12B), B91–B96.

OFFERMANS, G.P., BIFERALE, L., BUZZICOTTI, M. & LINKMANN, M. 2018 A priori study of the subgrid energy transfers for small-scale dynamo in kinematic and saturation regimes. *Phys. Plasmas* **25** (12), 122307.

OUGHTON, S. & MATTHAEUS, W.H. 2020 Critical balance and the physics of magnetohydrodynamic turbulence. *Astrophys. J.* **897**, 37.

OUGHTON, S., PRIEST, E.R. & MATTHAEUS, W.H. 1994 The influence of a mean magnetic field on three-dimensional MHD turbulence. *J. Fluid Mech.* **280**, 95–117.

PARKER, E.N. 1957 Sweet's mechanism for merging magnetic fields in conducting fluids. *J. Geophys. Res.* **62** (4), 509–520.

PATTERSON, G.S. & ORSZAG, S.A. 1971 Spectral calculations of isotropic turbulence: efficient removal of aliasing interactions. *Phys. Fluids* **14**, 2538–2541.

PETROSYAN, A., BALOGH, A., GOLDSTEIN, M.L., LÉORAT, J., MARSCH, E., PETROVAY, K., ROBERTS, B., VON STEIGER, R. & VIAL, J.C. 2010 Turbulence in the solar atmosphere and solar wind. *Space Sci. Rev* **156**, 135–238.

PLUNIAN, F., STEPANOV, R. & FRICK, P. 2013 Shell models of magnetohydrodynamic turbulence. *Phys. Rep.* **523** (1), 1–60.

POPE, S.B. 2000 *Turbulent Flows*. Cambridge University Press.

RODRIGUEZ IMAZIO, P., MARTIN, L.N., DMITRUK, P. & MININNI, P.D. 2013 Intermittency in Hall-magnetohydrodynamics with a strong guide field. *Phys. Plasmas* **20**, 052506.

SAHOO, G., PERLEKAR, P. & PANDIT, R. 2011 Systematics of the magnetic-Prandtl-number dependence of homogeneous, isotropic magnetohydrodynamic turbulence. *New J. Phys.* **13**, 013036.

SALEM, C., MANGENEY, A., BALE, S.D. & VELTRI, P. 2009 Solar wind magnetohydrodynamics turbulence: anomalous scaling and role of intermittency. *Astrophys. J.* **702**, 537–553.

SCHEKOCHIHIN, A.A. 2022 MHD turbulence: a biased review. *J. Plasma Phys.* **88** (5), 155880501.

SCHMIDT, W. 2015 Large eddy simulations in astrophysics. *Liv. Rev. Comput. Astrophys.* **1**, 2.

SHEBALIN, J.V., MATTHAEUS, W.H. & MONTGOMERY, D. 1983 Anisotropy in MHD turbulence due to a mean magnetic field. *J. Plasma Phys.* **29**, 525–547.

SMAGORINSKY, J. 1963 General circulation experiments with the primitive equations. *Mon. Weath. Rev.* **91**, 99.

SPYKSMA, K., MAGCALAS, M. & CAMPBELL, N. 2012 Quantifying effects of hyperviscosity on isotropic turbulence. *Phys. Fluids* **24**.

SWEET, P.A. 1958 The neutral point theory of solar flares. In *Electromagnetic Phenomena in Cosmical Physics* (ed. B. Lehnert), p. 123. Cambridge University Press.

TEACA, B., VERMA, M.K., KNAEPEN, B. & CARATI, D. 2009 Energy transfer in anisotropic magnetohydrodynamic turbulence. *Phys. Rev.* E **79**, 046312.

TOBIAS, S.M. & CATTANEO, F. 2013 Shear-driven dynamo waves at high magnetic Reynolds number. *Nature* **497**, 463–465.

VELA-MARTÍN, A. 2022 Subgrid-scale models of isotropic turbulence need not produce energy backscatter. *J. Fluid Mech.* **937**, A14.

VELTRI, P. 1999 MHD turbulence in the solar wind: self-similarity, intermittency and coherent structures. *Plasma Phys. Control. Fusion* **41**, A787–A795.

VERMA, M.K. 2004 Statistical theory of magnetohydrodynamic turbulence: recent results. *Phys. Rep.* **401**, 229–380.

VERMA, M.K. 2019 *Energy Transfers in Fluid Flows: Multiscale and Spectral Perspectives*. Cambridge University Press.

VLAYKOV, D.G., GRETE, P., SCHMIDT, W. & SCHLEICHER, D.R.G. 2016 A nonlinear structural subgrid-scale closure for compressible MHD. I. Derivation and energy dissipation properties. *Phys. Plasmas* **23**, 062316.

VREMAN, B., GEURTS, B. & KUERTEN, H. 1996 Large-eddy simulation of the turbulent mixing layer using the Clark model. *Theor. Comput. Fluid Dyn.* **8**, 309–324.

VREMAN, B., GEURTS, B. & KUERTEN, H. 1997 Large-eddy simulation of the turbulent mixing layer. *J. Fluid Mech.* **339**, 357–390.

WALEFFE, F. 1993 Inertial transfers in the helical decomposition. *Phys. Fluids* A **5**, 667.

WAN, M., OSMAN, K.T., MATTHAEUS, W.H. & OUGHTON, S. 2012 Investigation of intermittency in magnetohydrodynamics and solar wind turbulence: scale-dependent kurtosis. *Astrophys. J.* **744**, 171.

WAN, M., OUGHTON, S., SERVIDIO, S. & MATTHAEUS, W.H. 2010 On the accuracy of simulations of turbulence. *Phys. Plasmas* **17**, 082308.

WEISS, N.O. & PROCTOR, M.R.E. 2014 *Magnetoconvection*. Cambridge University Press.

YANG, P.-F., ZHOU, Z.D., XU, H. & HE, G.W. 2023 Strain self-amplification is larger than vortex stretching due to an invariant relation of filtered velocity gradients. *J. Fluid Mech.* **955**, A15.

YANG, Y., LINKMANN, M., BIFERALE, L. & WAN, M. 2021 Effects of forcing mechanisms on the multiscale properties of magnetohydrodynamics. *Astrophys. J.* **909** (2), 175.

YOSHIMATSU, K., SCHNEIDER, K., OKAMOTO, N., KAWAHARA, Y. & FARGE, M. 2011 Intermittency and geometrical statistics of three-dimensional homogeneous magnetohydrodynamic turbulence: a wavelet viewpoint. *Phys. Plasmas* **18**, 092304.

ZHOU, Y., MATTHAEUS, W.H. & DMITRUK, P. 2004 Magnetohydrodynamic turbulence and time scales in astrophysical and space plasmas. *Rev. Mod. Phys.* **76**, 1015–1035.

ZHOU, Y. & VAHALA, G. 1991 Aspects of subgrid modelling and large-eddy simulation of magnetohydrodynamic turbulence. *J. Plasma Phys.* **45** (2), 239–249.